

Supplementary Materials B: Simulations and Real-Data Case Studies

1 Varying Parameters

In this section, we explore the effect of varying parameters on estimating source emission rate, location, measurement error variance, background concentration, and diffusion parameters. Each subsection focuses on varying a different factor ((a) WDC: wind direction coverage [degrees°], (b) DPV: dispersion parameter values, (c) SER: source emission rate [kg/s], (d) DTS: distance between the source and sensors [m], (e) OPS: number of observations per sensor, and (f) SL: sensor layout.) while all other factors are fixed. We define low (L), medium (M), and high (H) levels, then perform a “main effects” analysis, changing each factor in turn from L to M and then to H, holding all other factors at level M. The level M conditions correspond to an emission source positioned at coordinates (50m, 50m, 5m) within a 110m × 110m square, emitting at a rate of 0.00039 kg/s, with all plume dispersion parameters set to 1.0. A grid of 36 evenly spaced sensors positioned downwind of the plume (see Figure 3), collects 100 measurements per sensor at a frequency of 1 Hz. An OU process simulates wind speeds with a mean of 6 m/s, and the wind direction varies every second, encompassing a 140° range as depicted in the left plot of Figure 1.

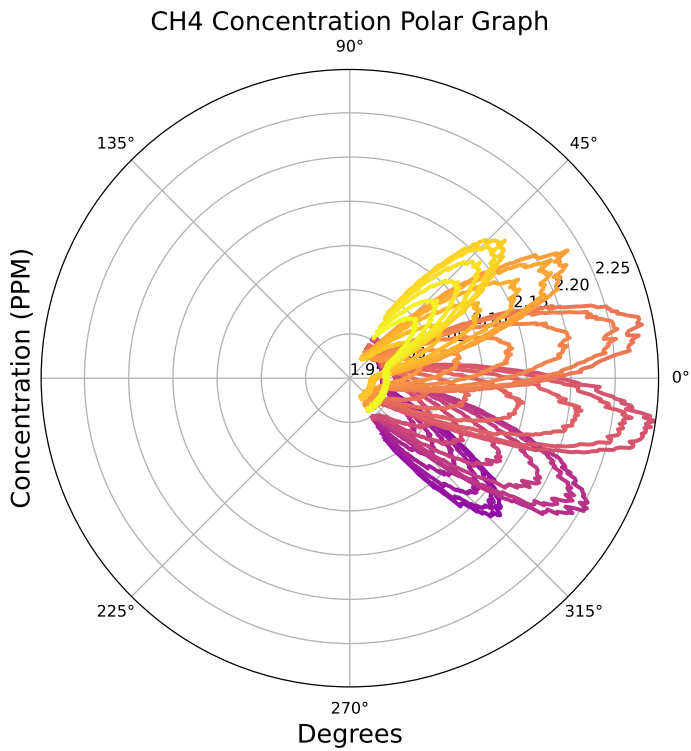


Figure 1: Polar plot of methane concentrations measured by the grid of 36 sensors. Wind direction coverage is 140° . Each line corresponds to a different sensor.

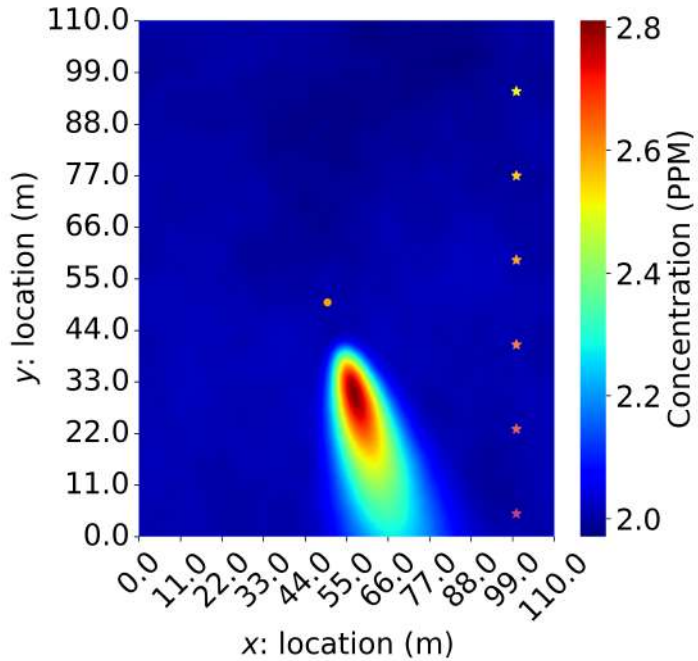


Figure 2: Source Gaussian plume model simulation at location $(50\text{m}, 50\text{m}, 5\text{m})$, with emission rate 0.00039 kg/s , and centered at sensor layout center. Background concentration is also included.

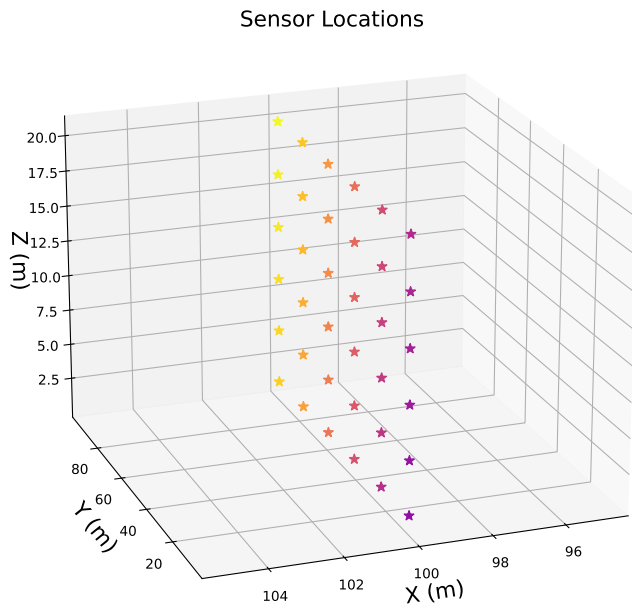


Figure 3: Sensor layout: grid of 36 equally spaced point sensors.

1.1 Varying the Wind Direction Coverage

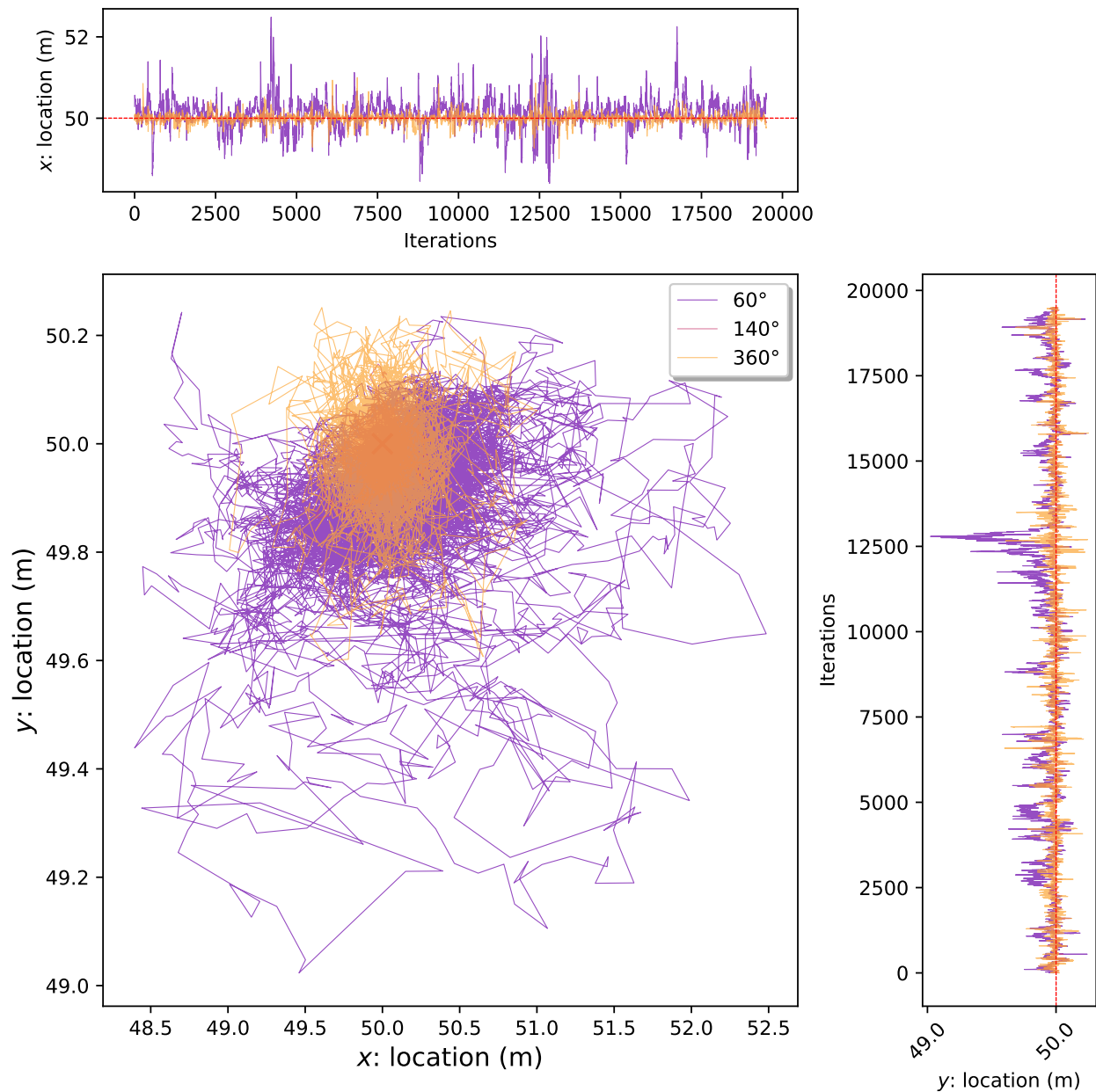


Figure 4: Source location estimation chains for varying wind direction coverage.

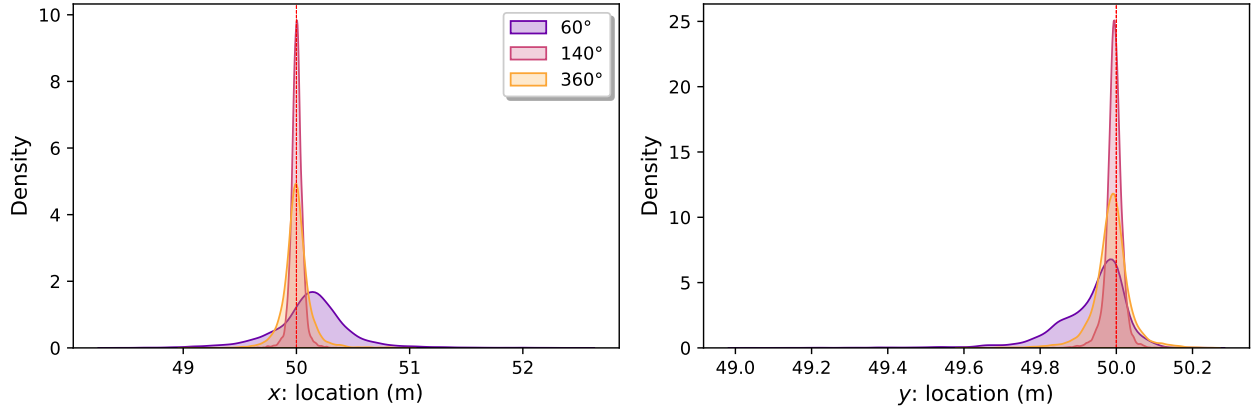


Figure 5: Source location estimation densities for varying wind direction coverage.

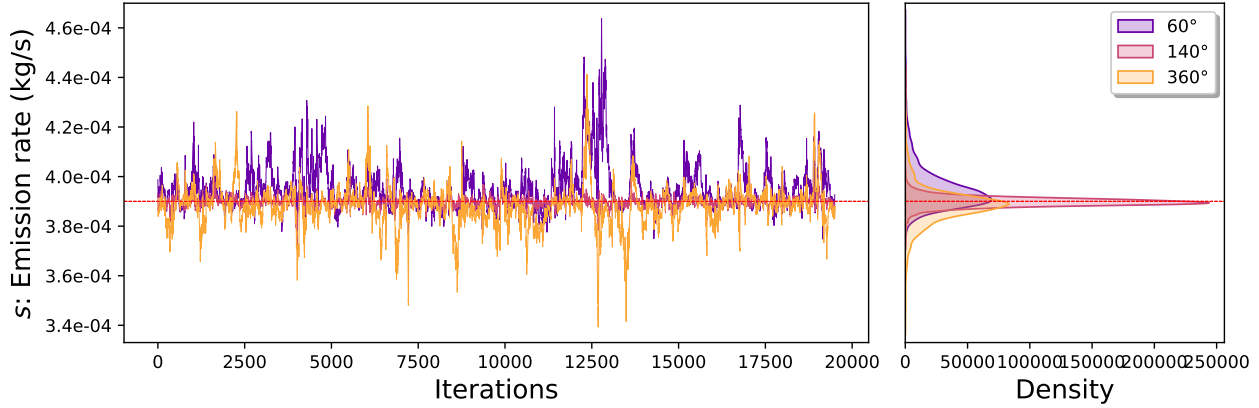


Figure 6: Source emission rate location estimation chains for varying wind direction coverage.

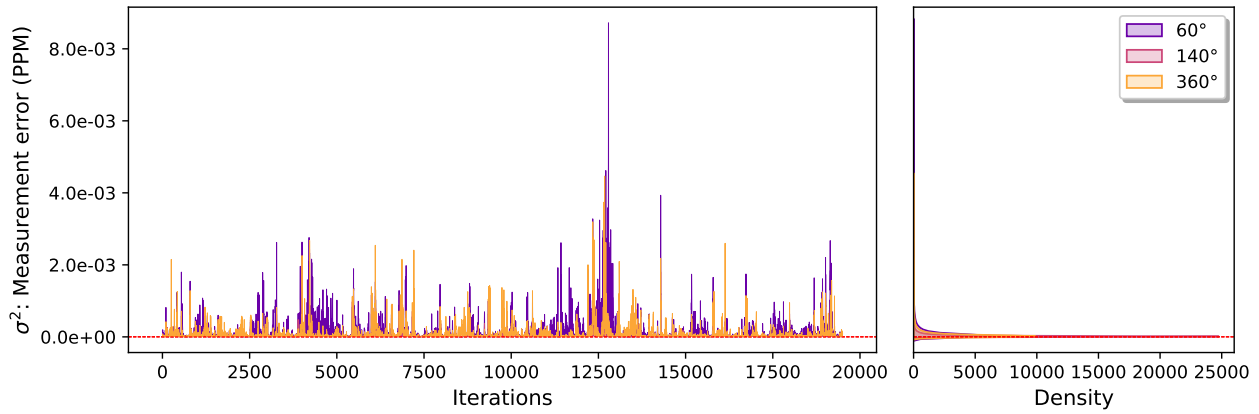


Figure 7: Sensor measurement error variance estimation chains for varying wind direction coverage.

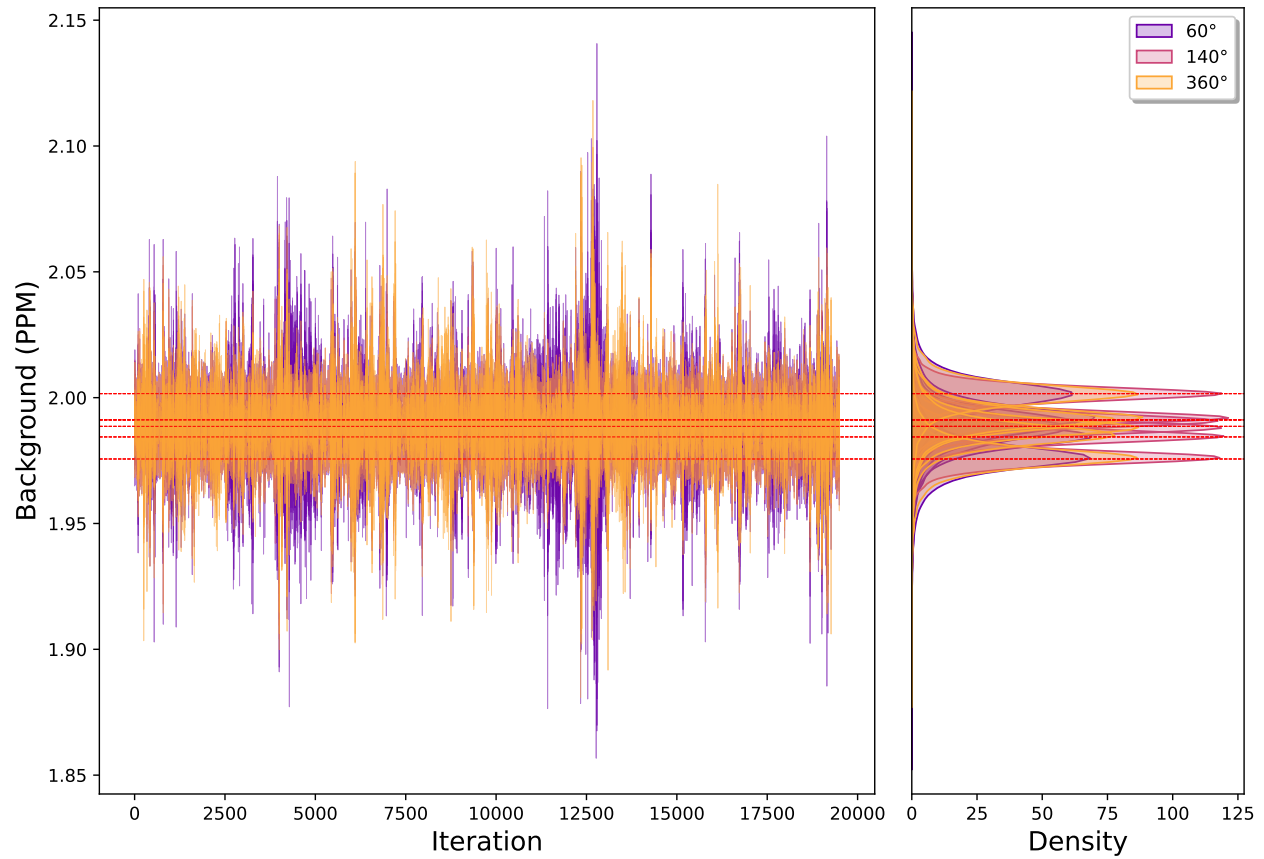


Figure 8: Background concentration estimation chains for varying wind direction coverage.

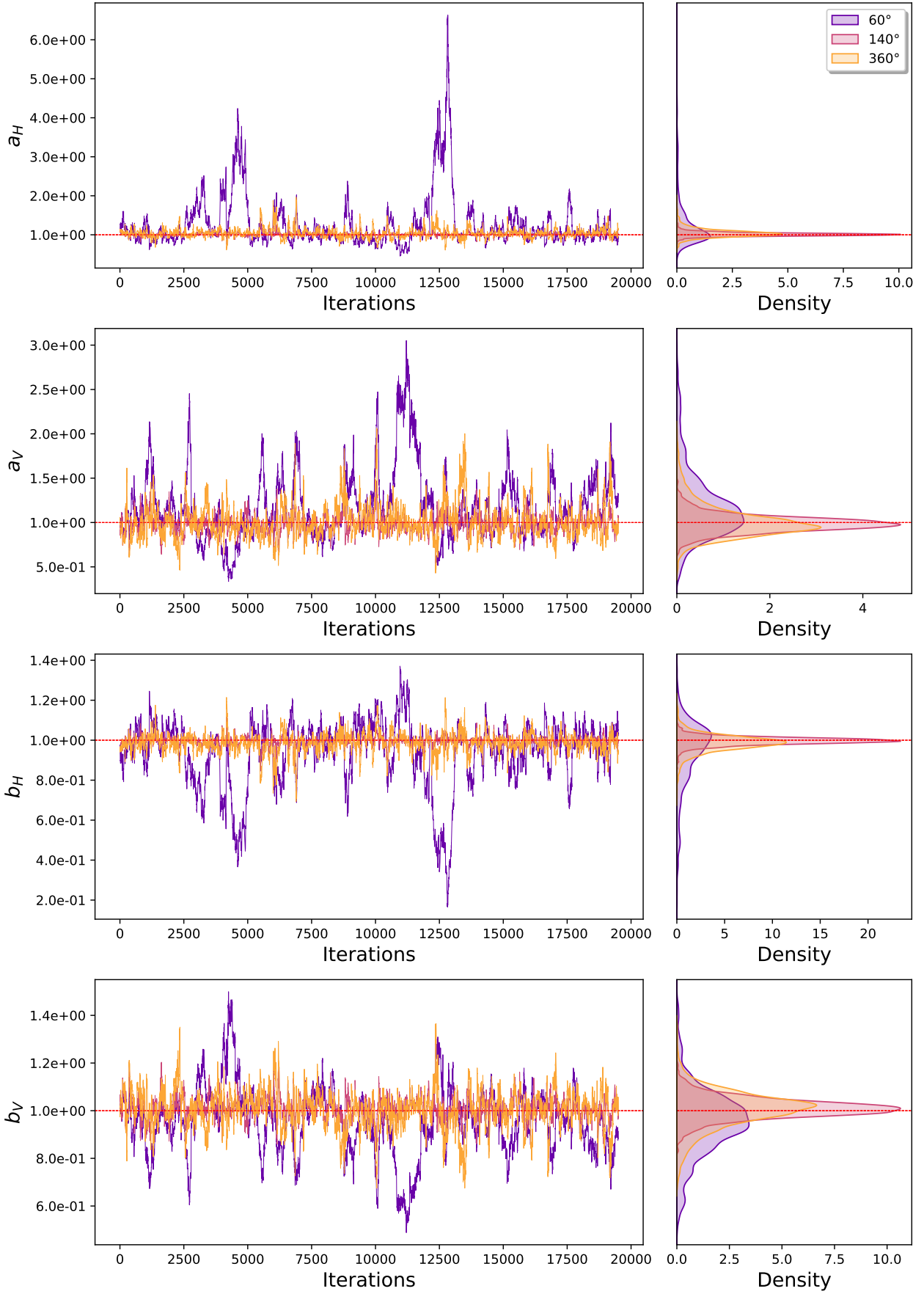


Figure 9: Diffusion parameter estimation chains for varying wind direction coverage.

In-depth simulation: Here we estimated the parameters for a range of different wind direction coverage. The sharp increase in estimation accuracy and reduction in estimation uncertainty corresponds to the change from a wind direction coverage that is smaller than the plume's width to a larger one. This is illustrated in Figure 12.

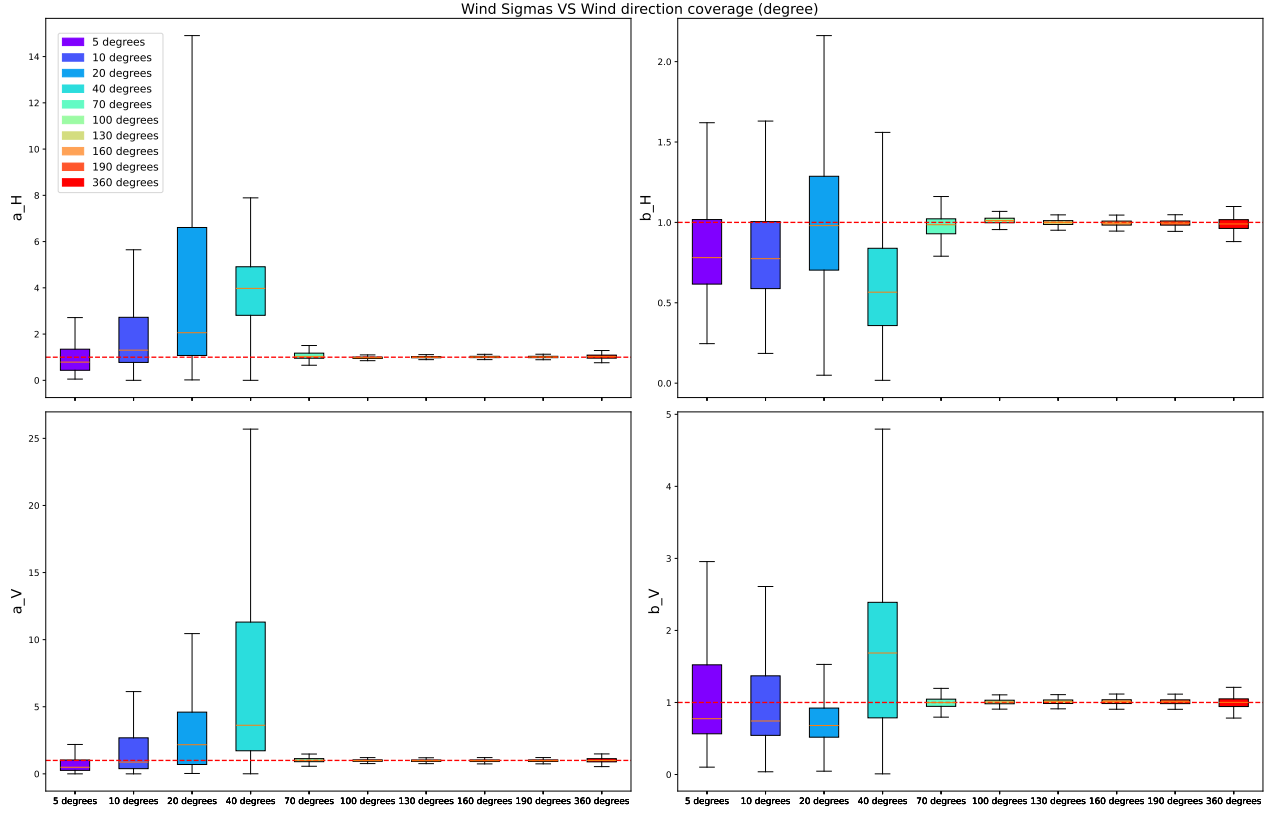


Figure 10: Dispersion parameters estimation for varying sensor layout.

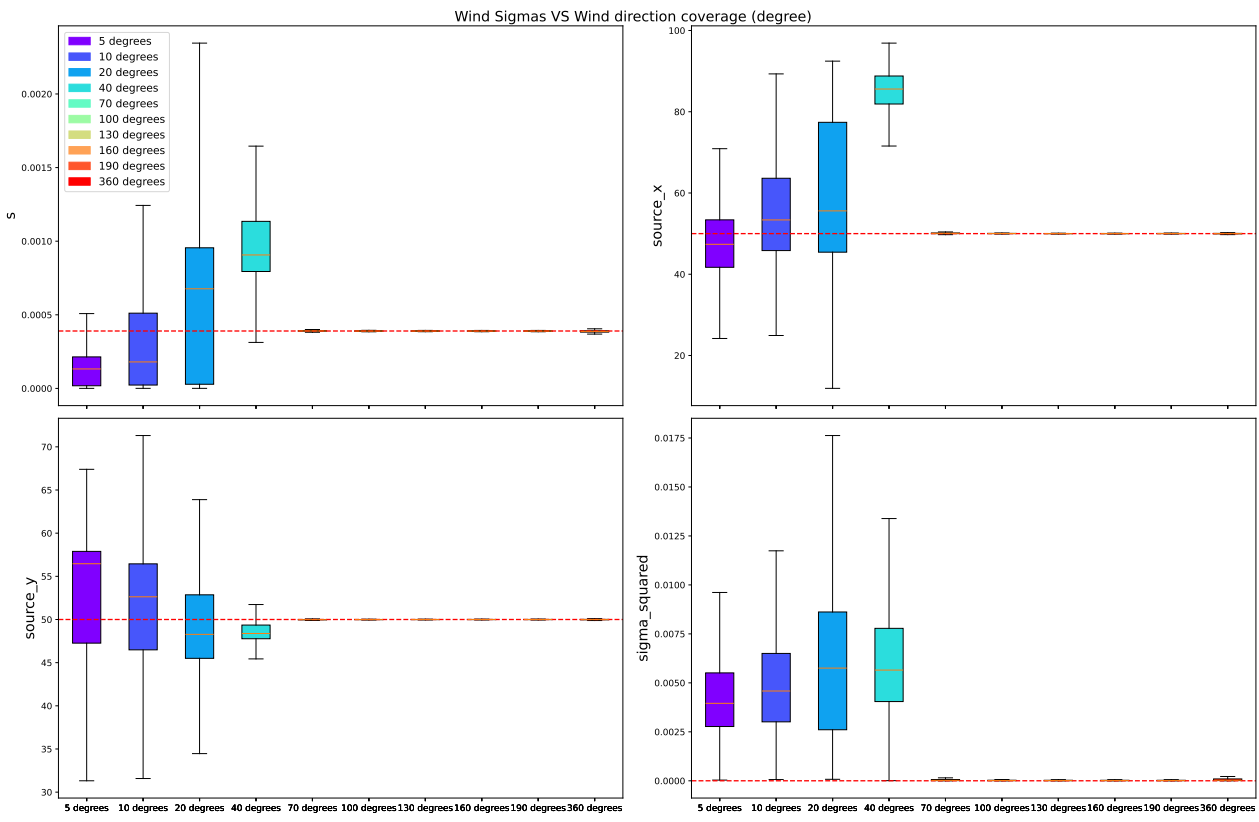


Figure 11: Source emission rate, location, and sensor measurement error variance estimation for varying wind sensor layout.

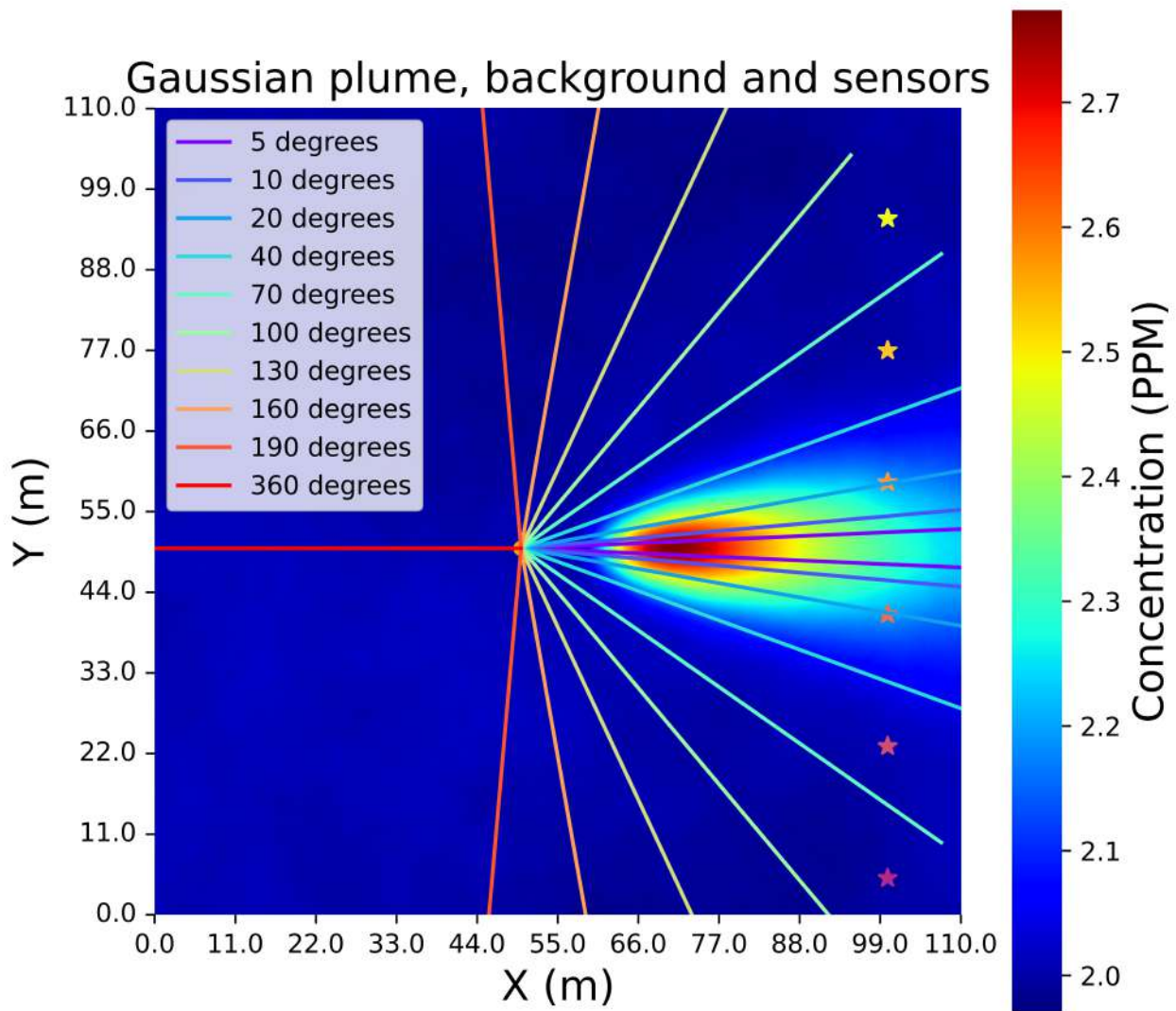


Figure 12: Visual representation of varying wind direction coverage with source location and sensor layout.

1.2 Varying the Dispersion Parameters' Value

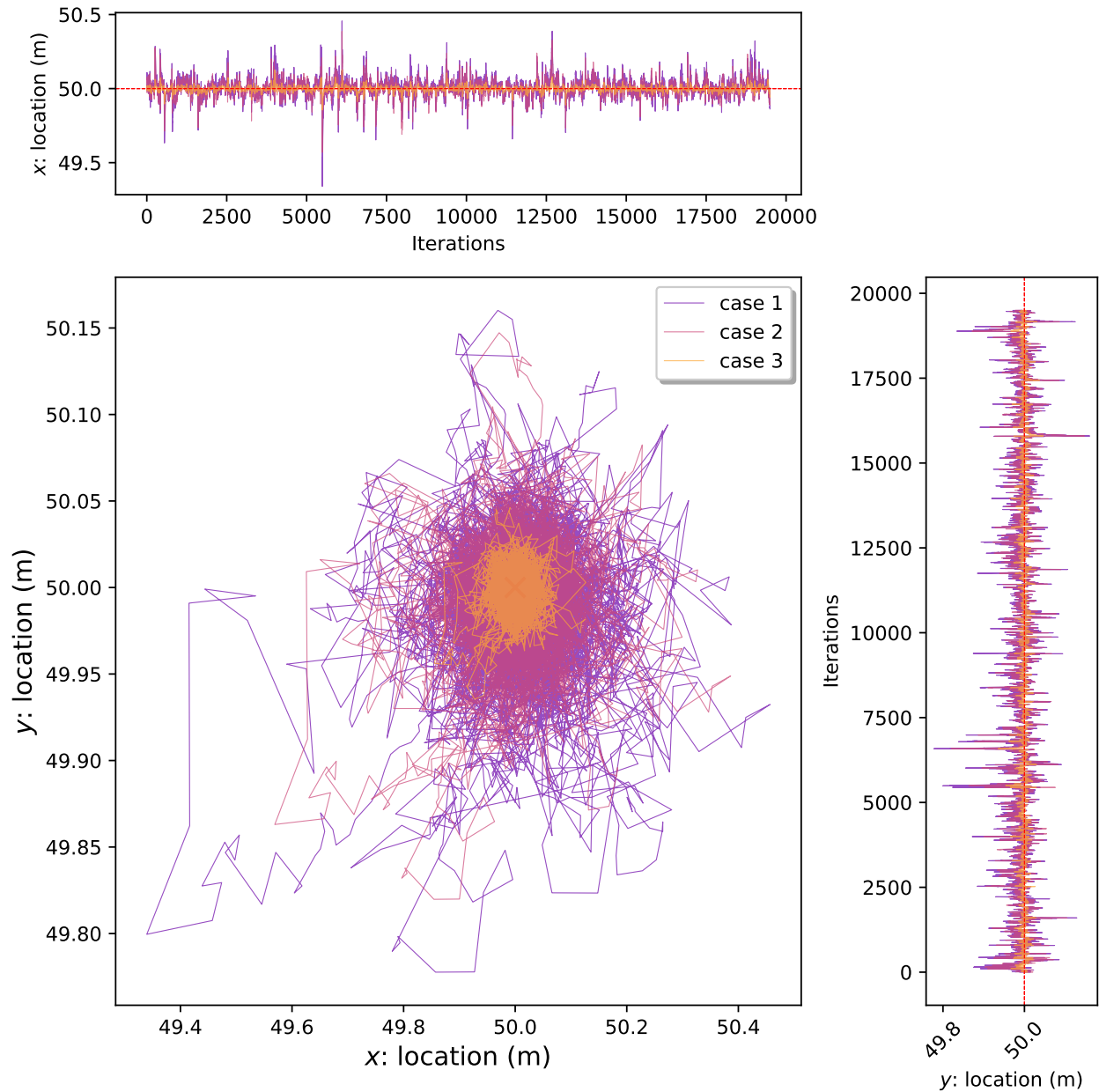


Figure 13: Source location estimation chains for varying dispersion parameter values.

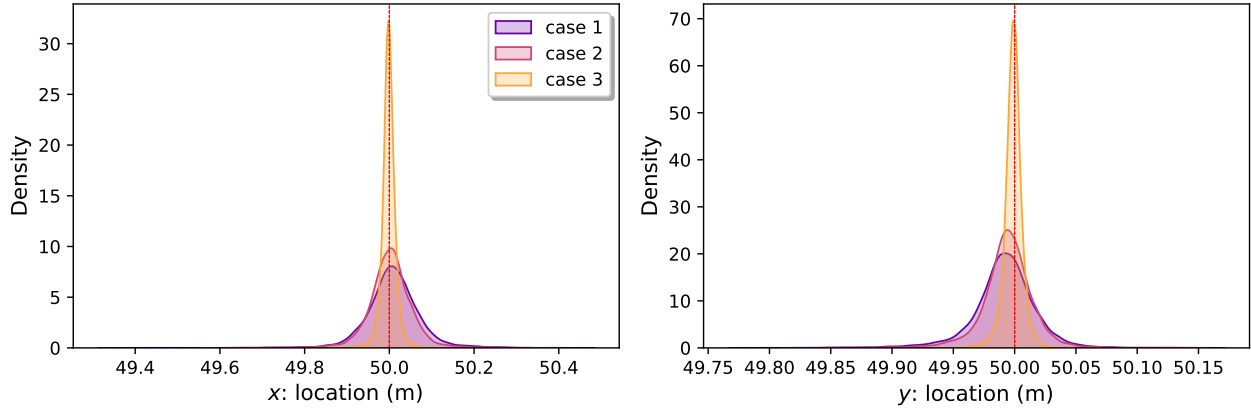


Figure 14: Source location estimation densities for varying dispersion parameter values.

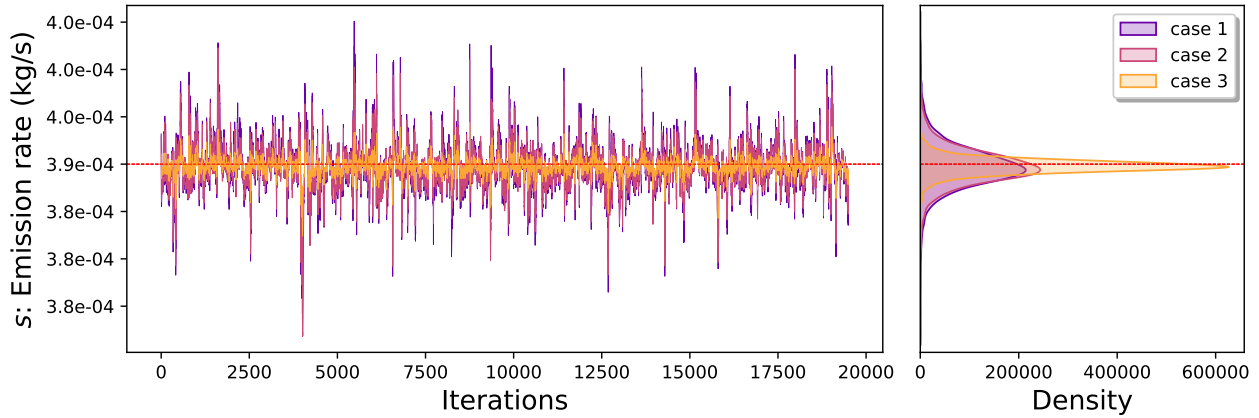


Figure 15: Source emission rate location estimation chains for varying dispersion parameter values.

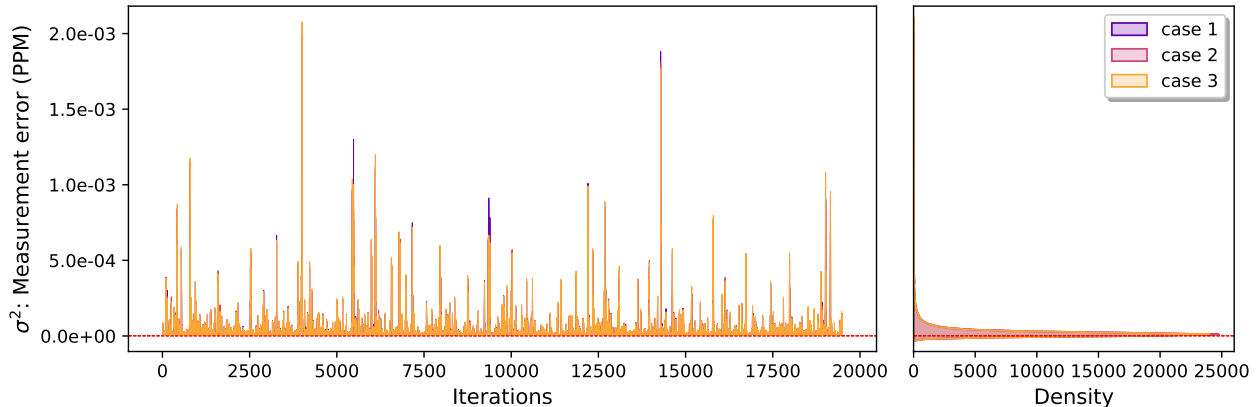


Figure 16: Sensor measurement error variance estimation chains for varying dispersion parameter values.

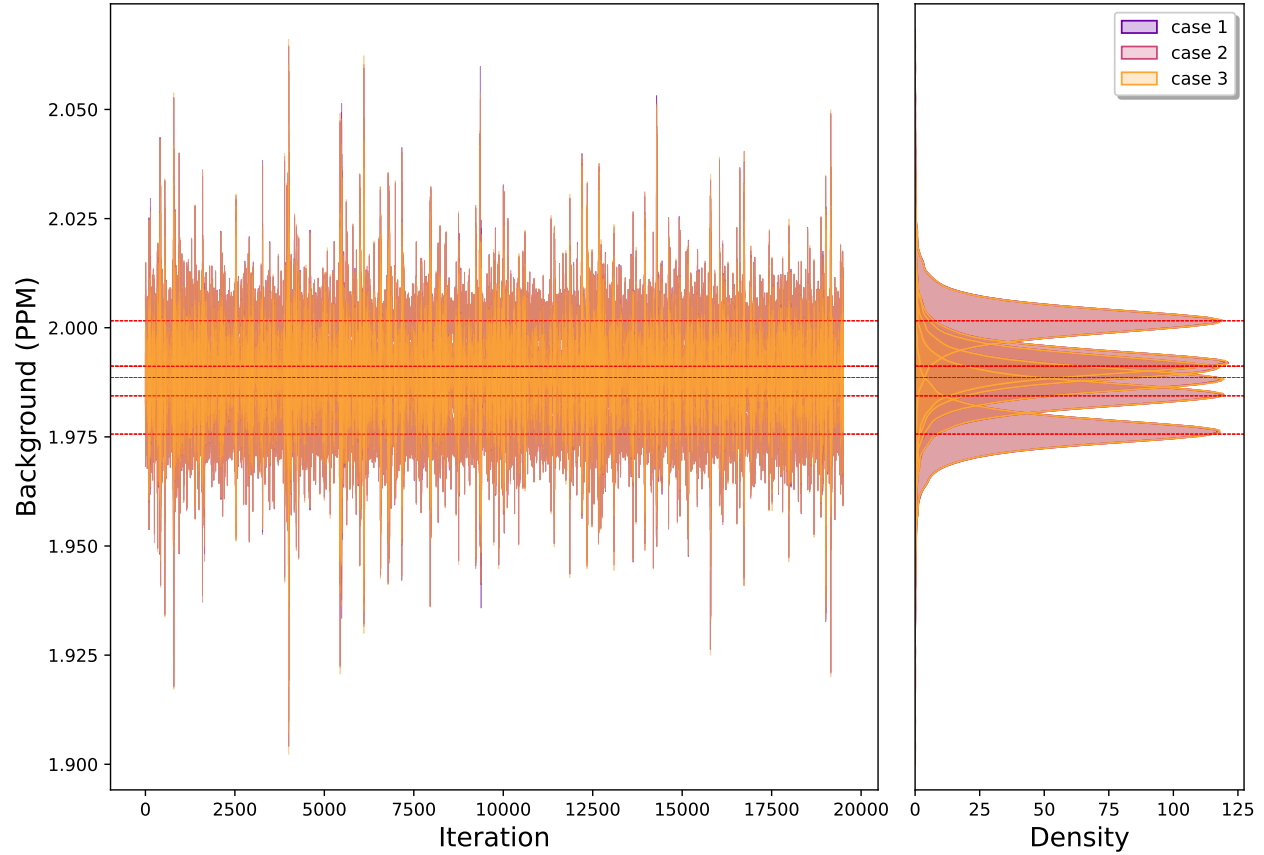


Figure 17: Background concentration estimation chains for varying dispersion parameter values.

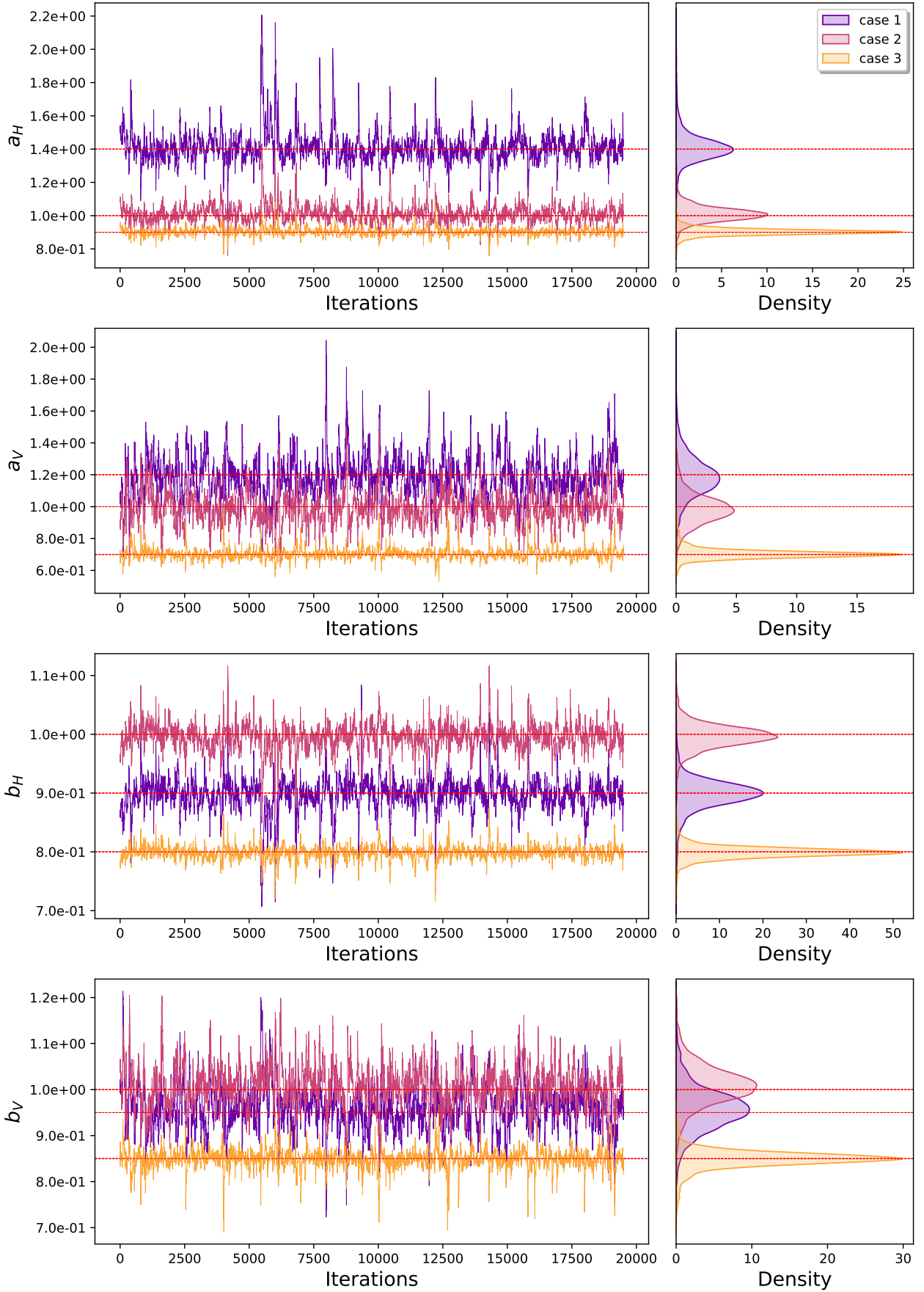


Figure 18: Diffusion parameter estimation chains for varying dispersion parameter values.

1.3 Varying the Source Emission Rate

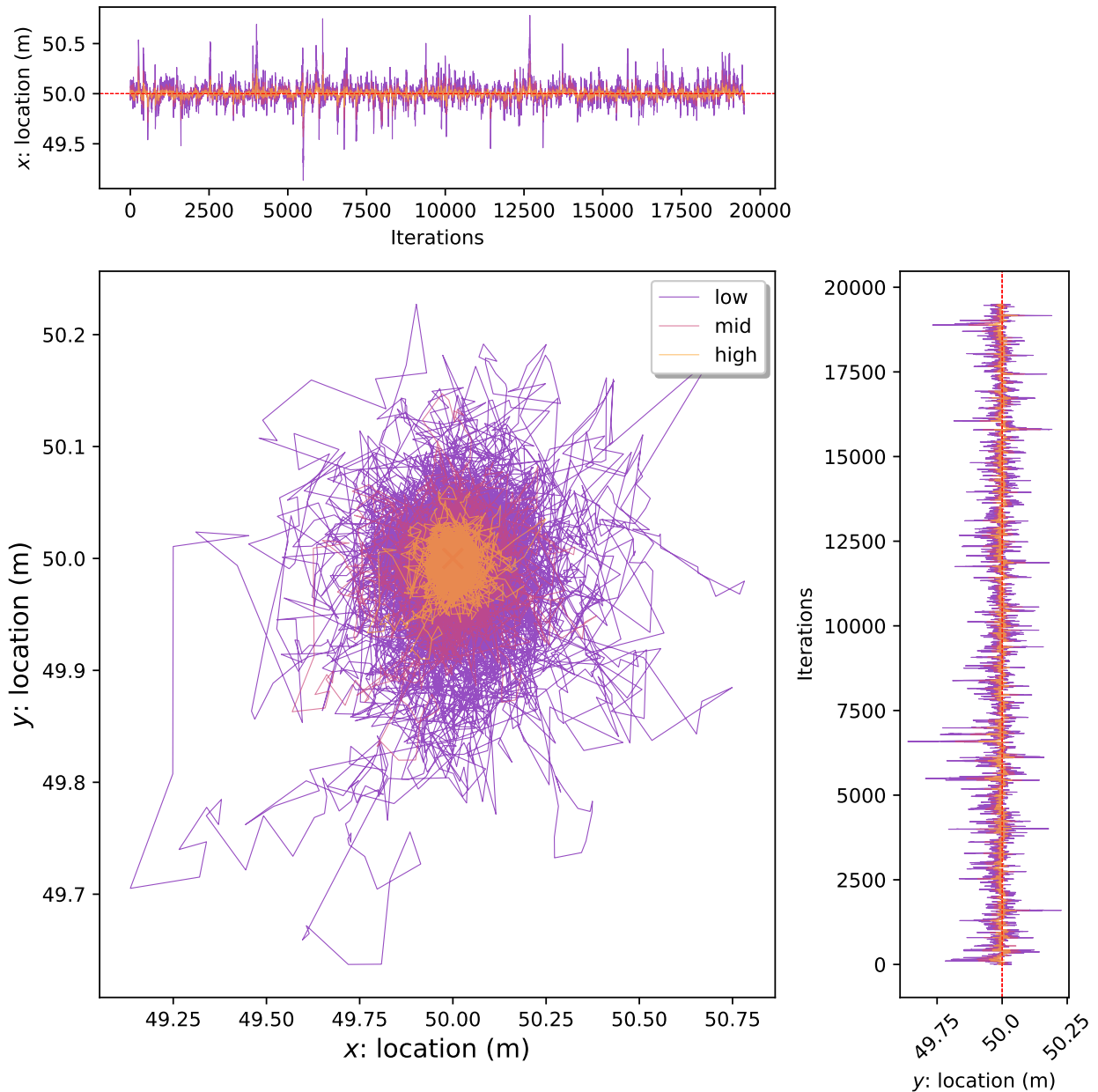


Figure 19: Source location estimation chains for varying source emission rate.

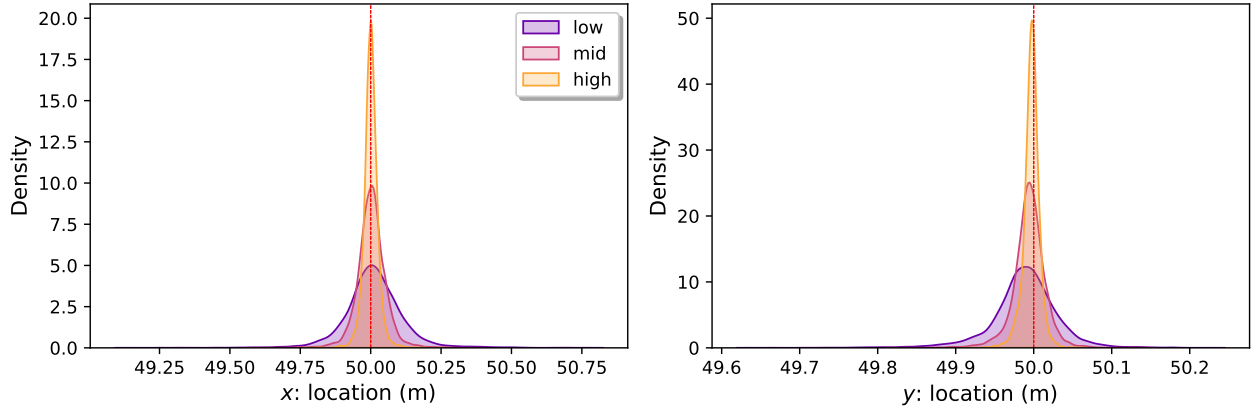


Figure 20: Source location estimation densities for varying source emission rate.

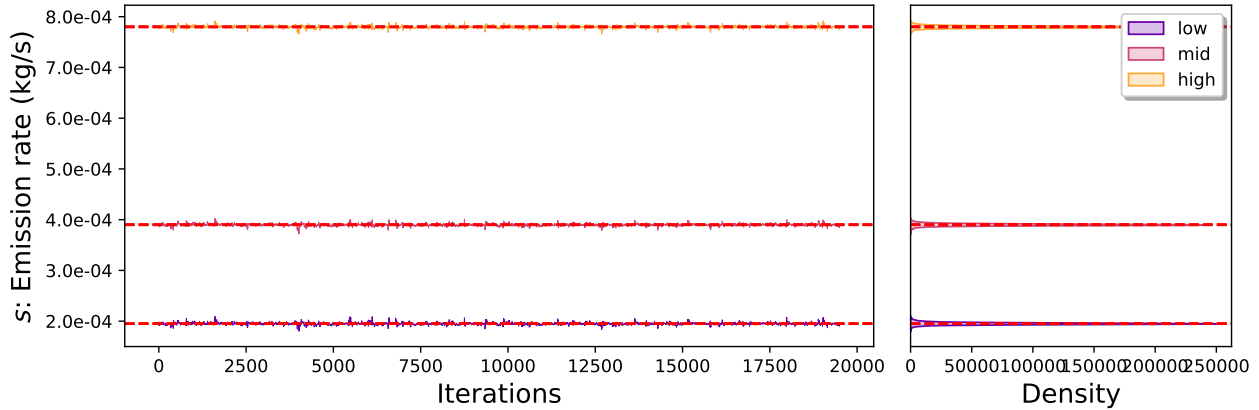


Figure 21: Source emission rate location estimation chains for varying source emission rate.

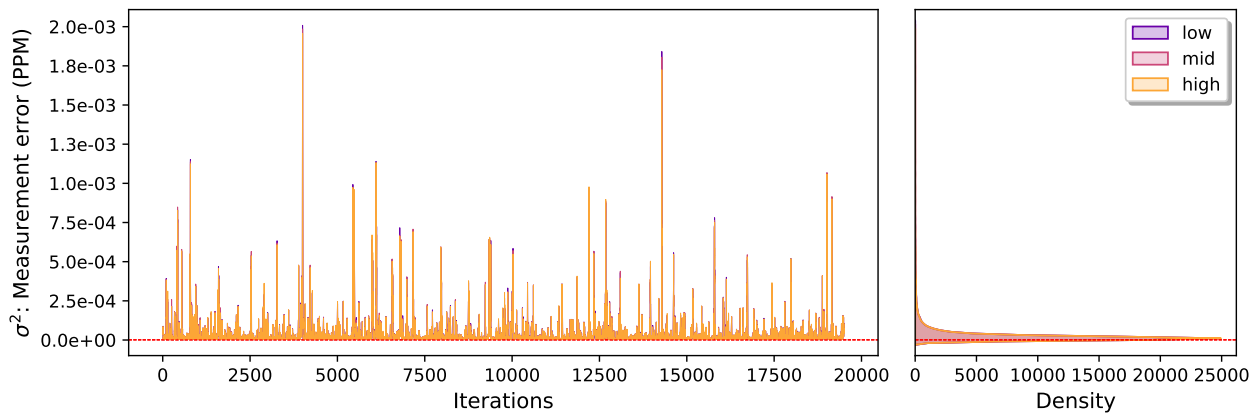


Figure 22: Sensor measurement error variance estimation chains for varying source emission rate.

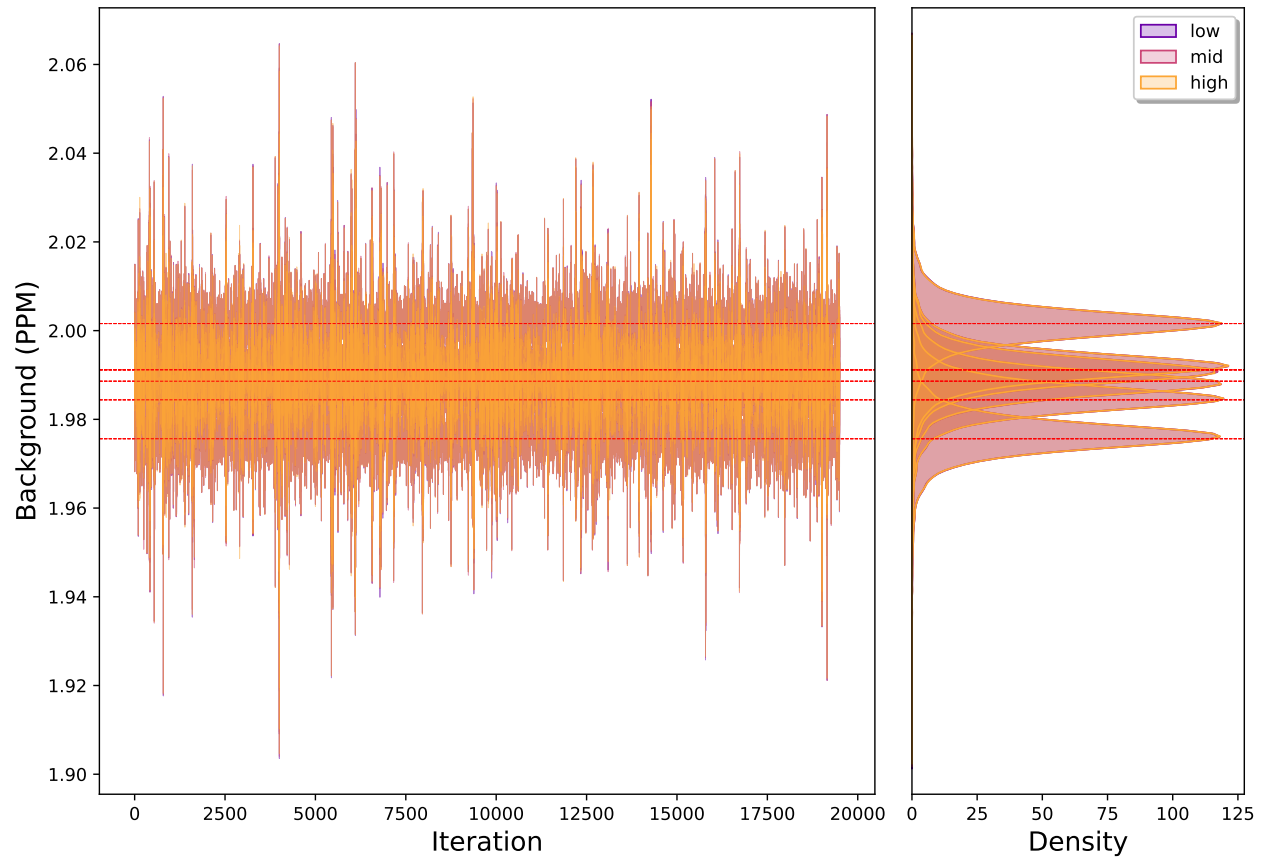


Figure 23: Background concentration estimation chains for varying source emission rate.

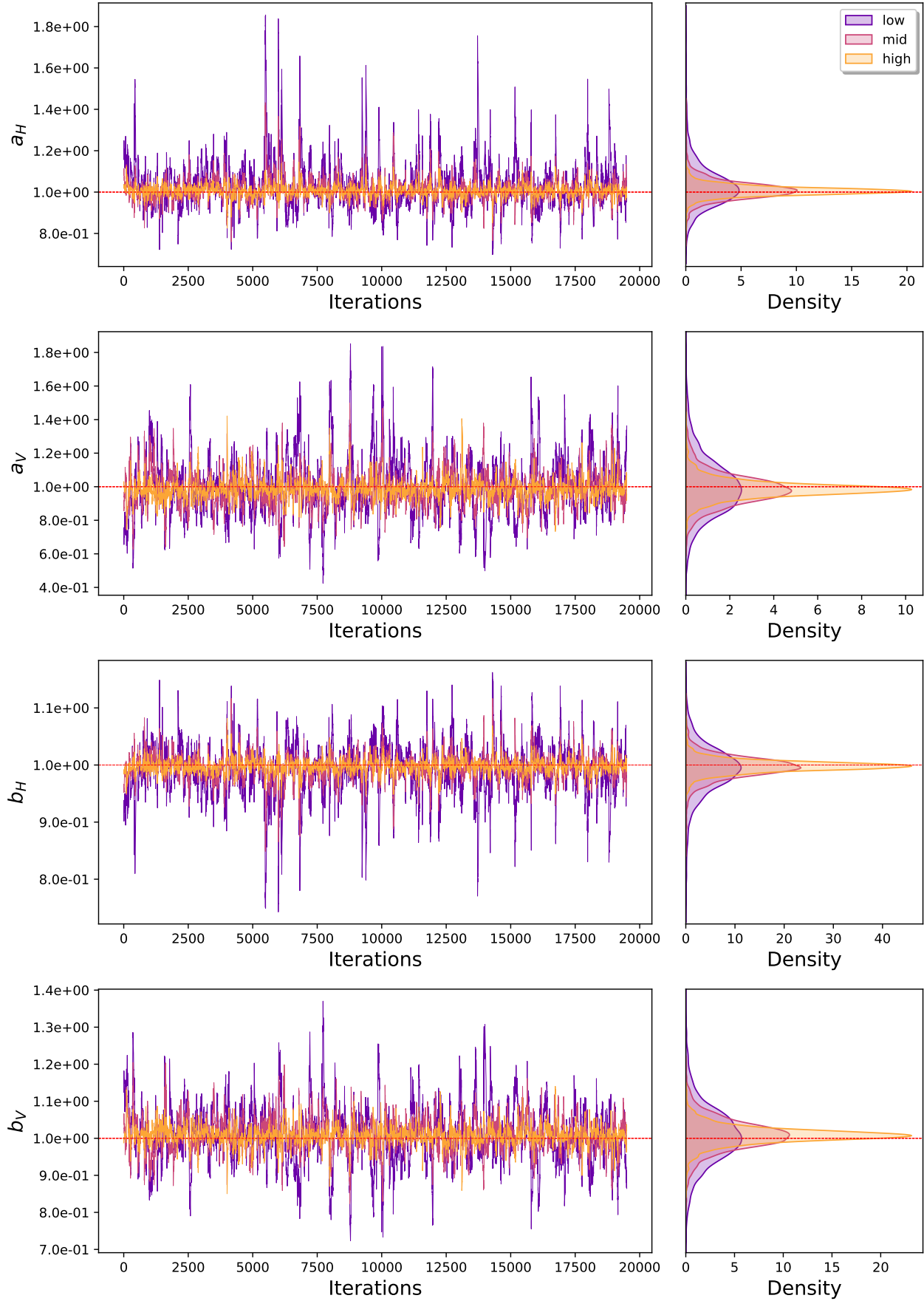


Figure 24: Diffusion parameter estimation chains for varying source emission rate.

1.4 Varying the Distance between the Source and Sensors

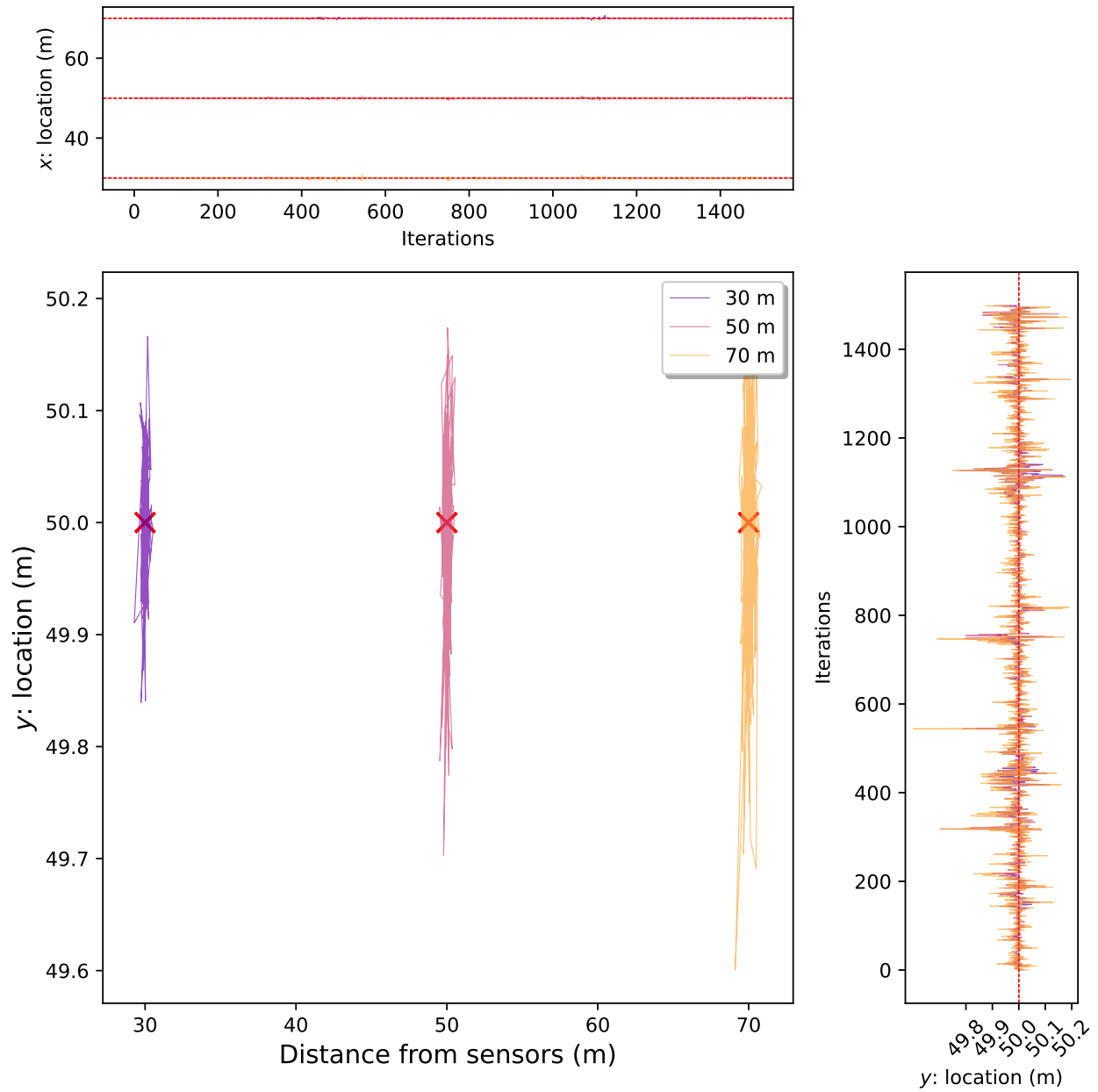


Figure 25: Source location estimation chains for varying distance between source and sensors.

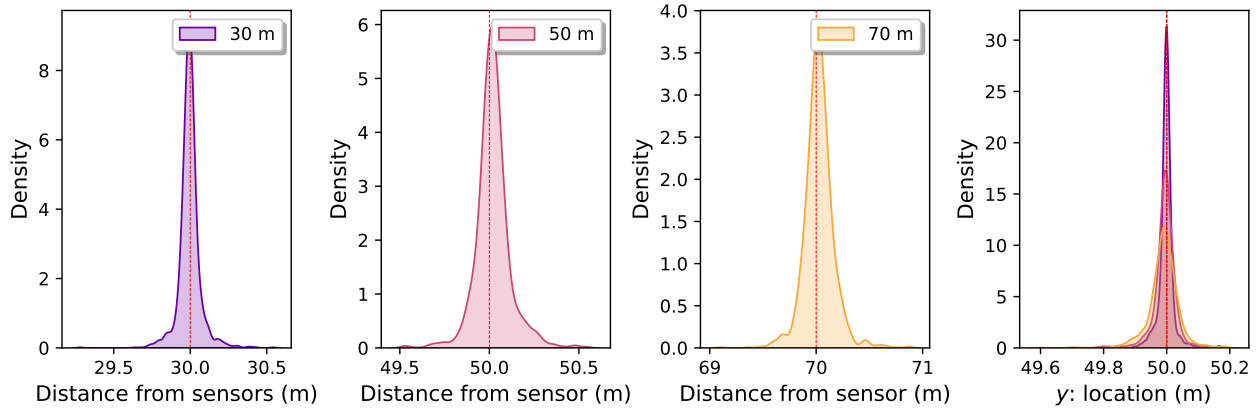


Figure 26: Source location estimation densities for varying distance between source and sensors.

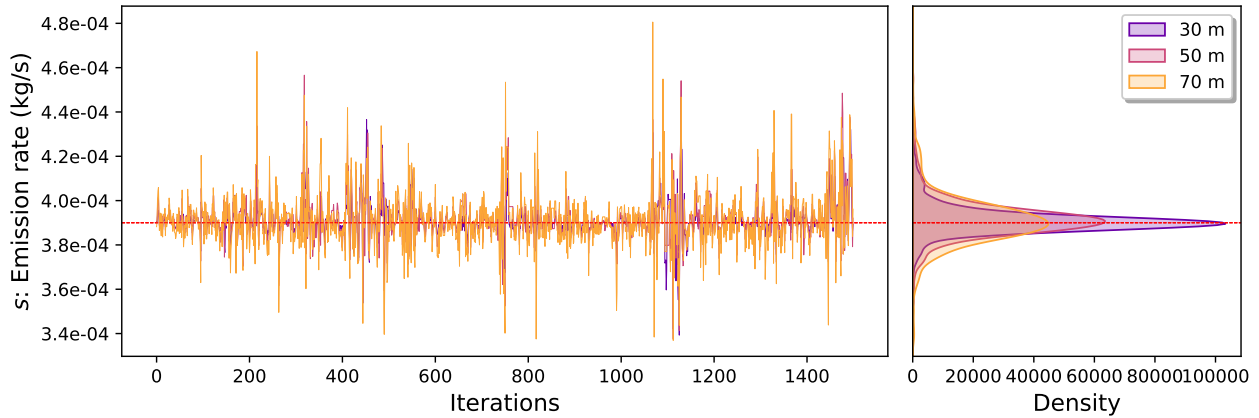


Figure 27: Source emission rate location estimation chains for varying distance between source and sensors.

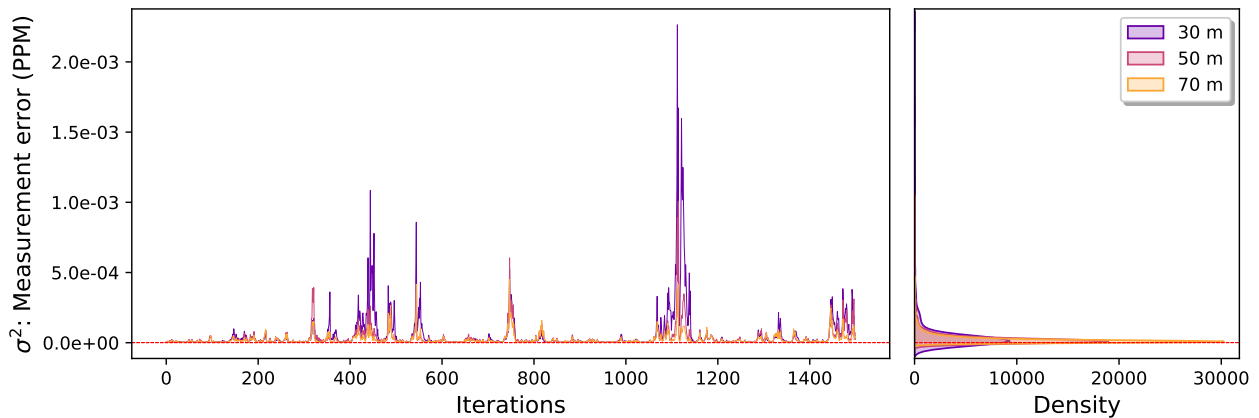


Figure 28: Sensor measurement error variance estimation chains for varying distance between source and sensors.

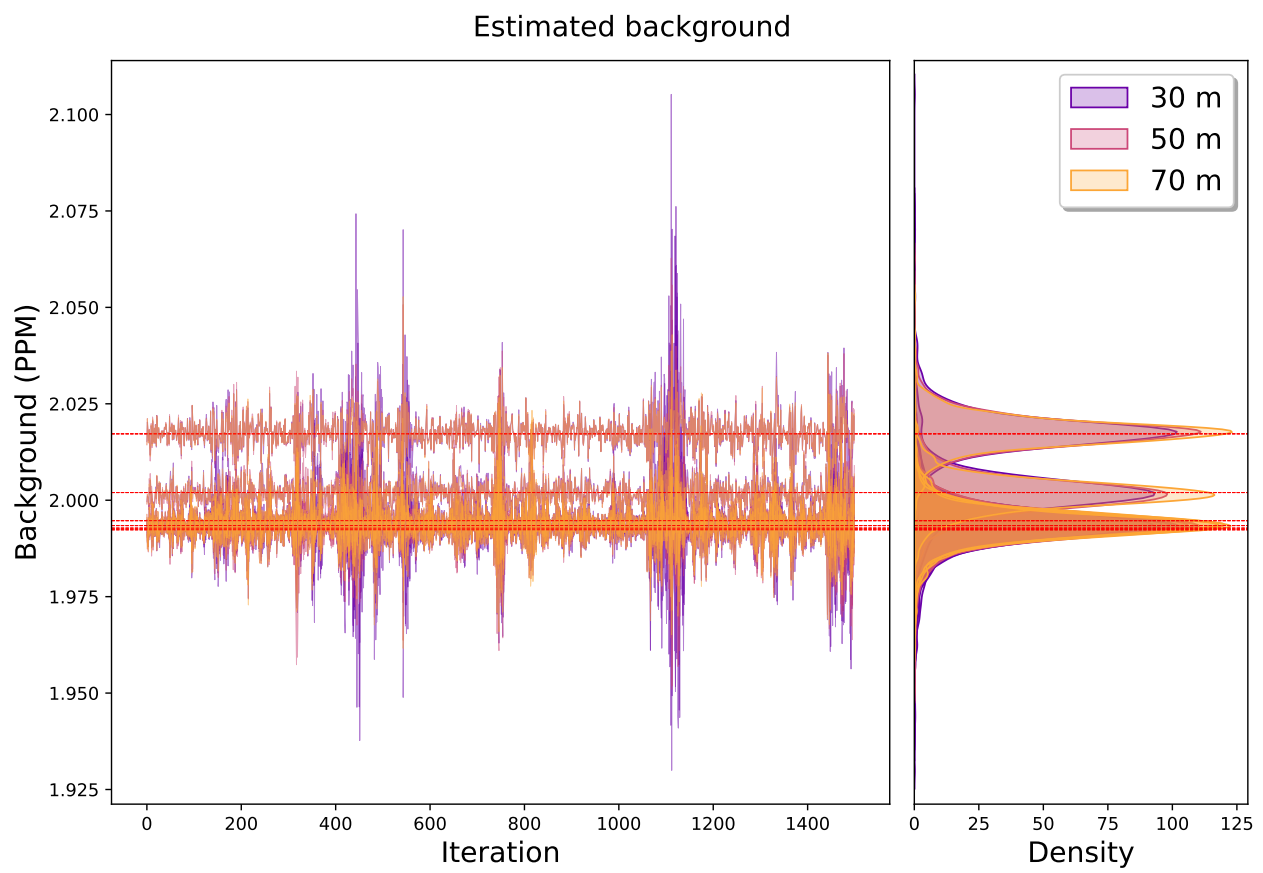


Figure 29: Background concentration estimation chains for varying distance between source and sensors.

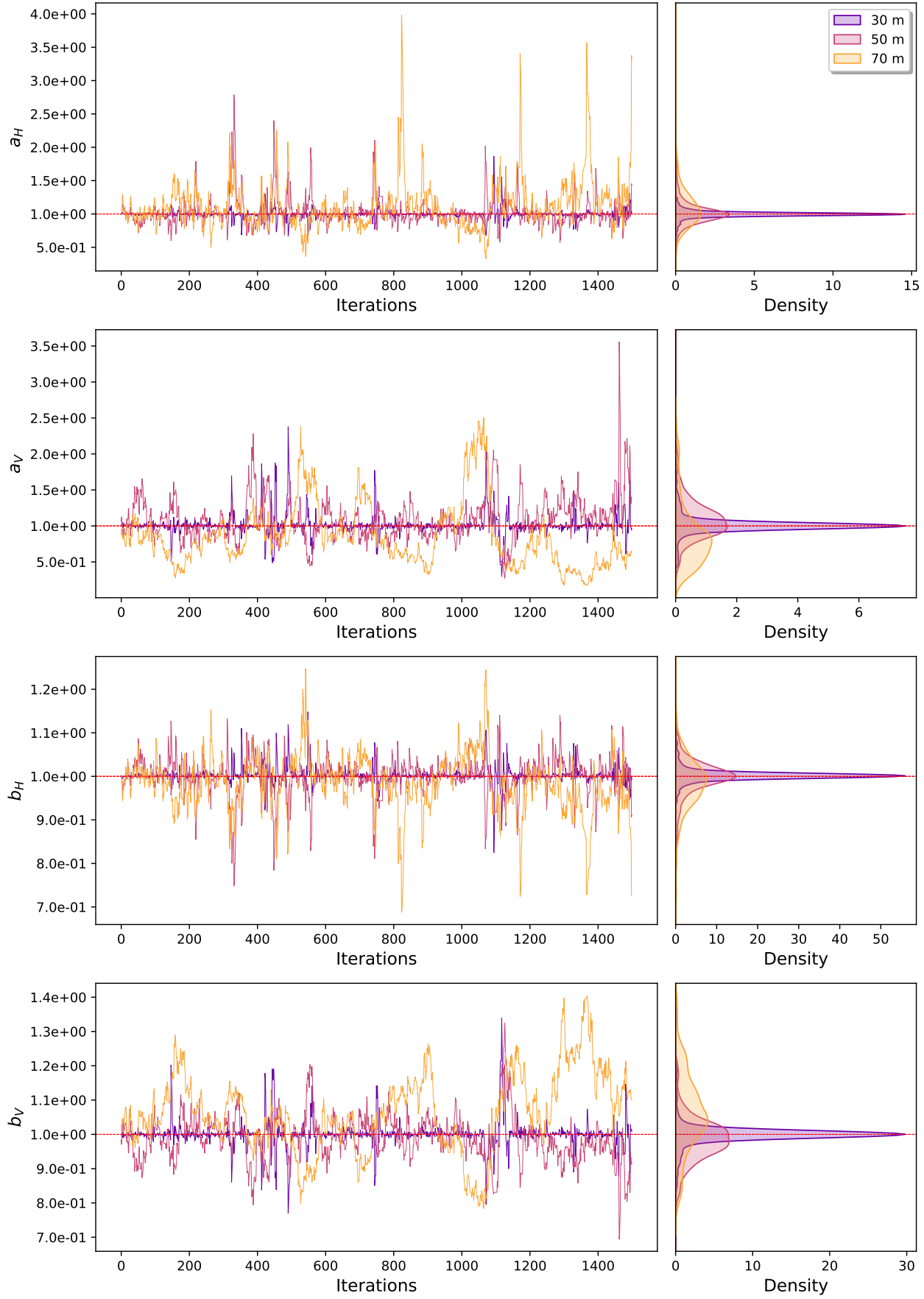


Figure 30: Diffusion parameter estimation chains for varying distance between source and sensors.

1.5 Varying the Number of Observation per Sensor

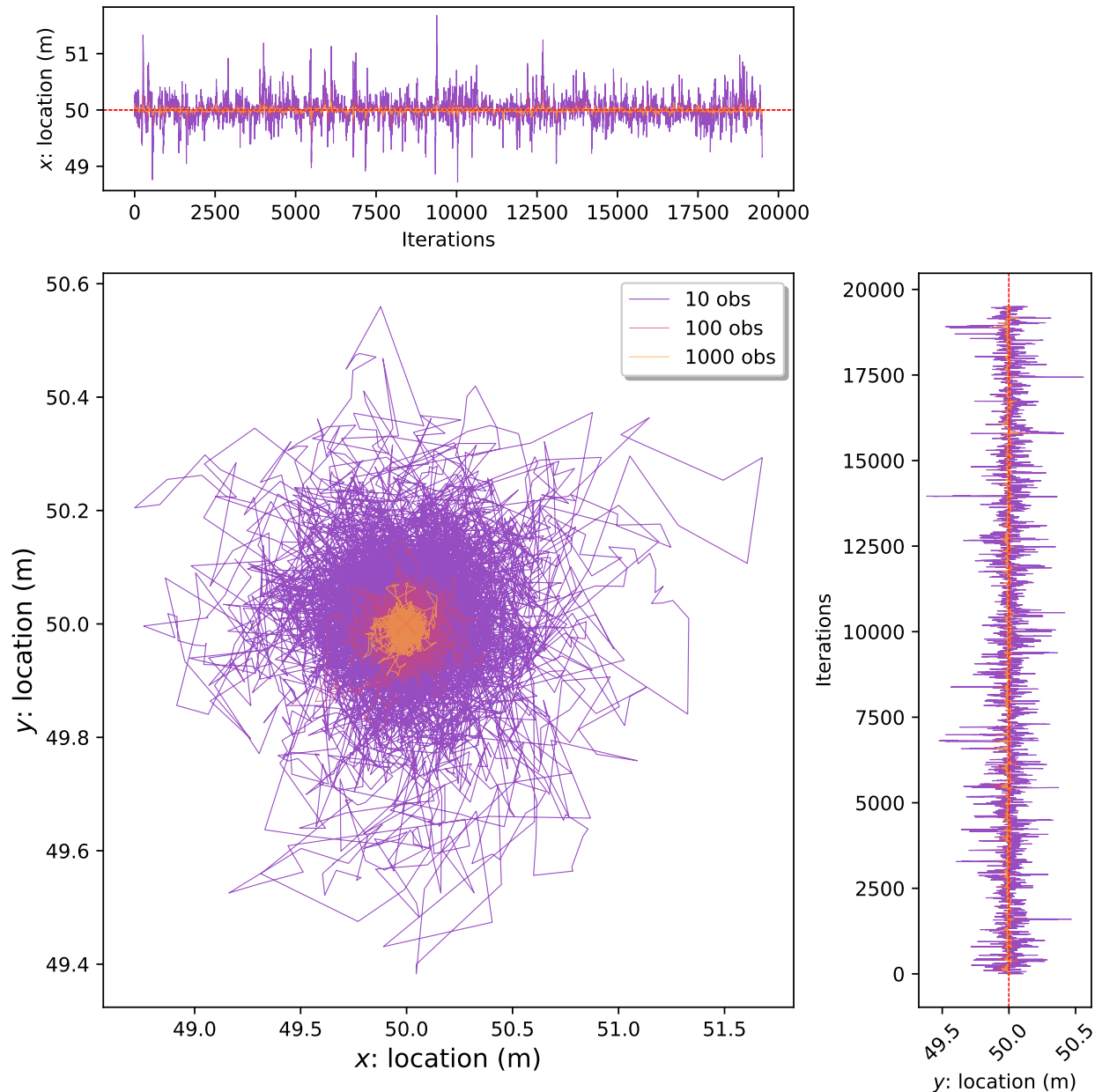


Figure 31: Source location estimation chains for varying number of observation per sensor.

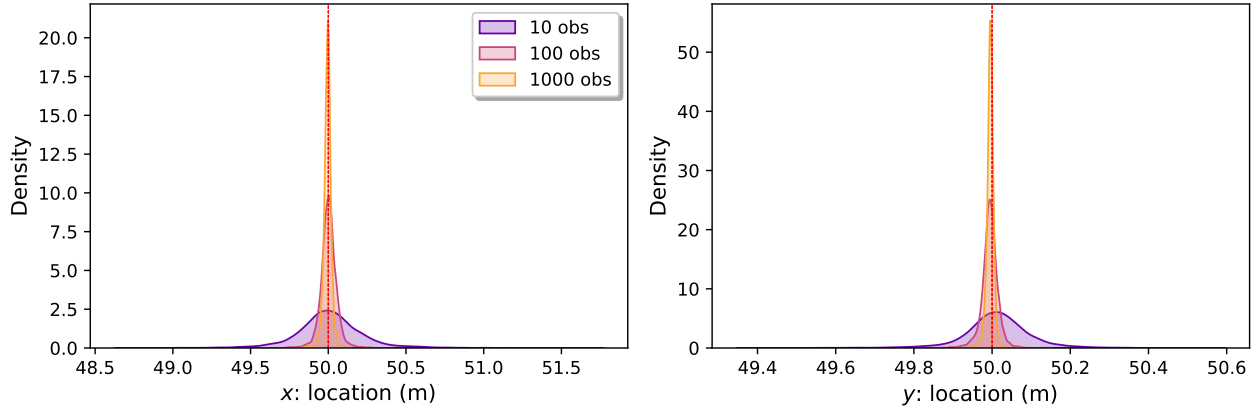


Figure 32: Source location estimation densities for varying number of observation per sensor.

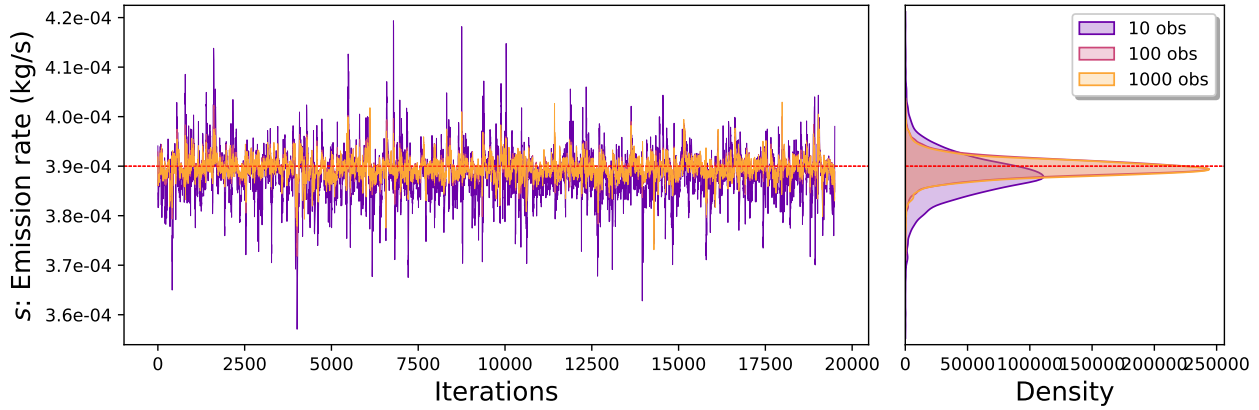


Figure 33: Source emission rate location estimation chains for varying number of observation per sensor.

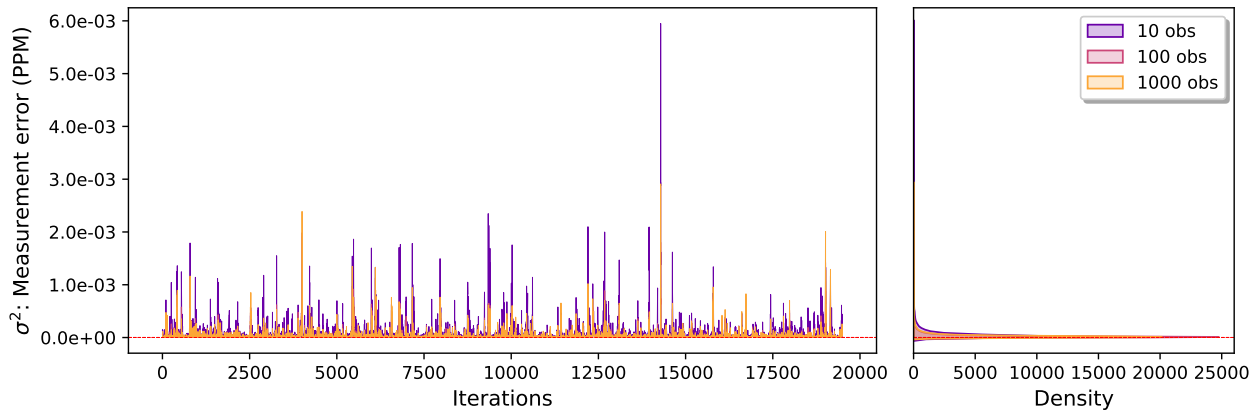


Figure 34: Sensor measurement error variance estimation chains for varying number of observation per sensor.

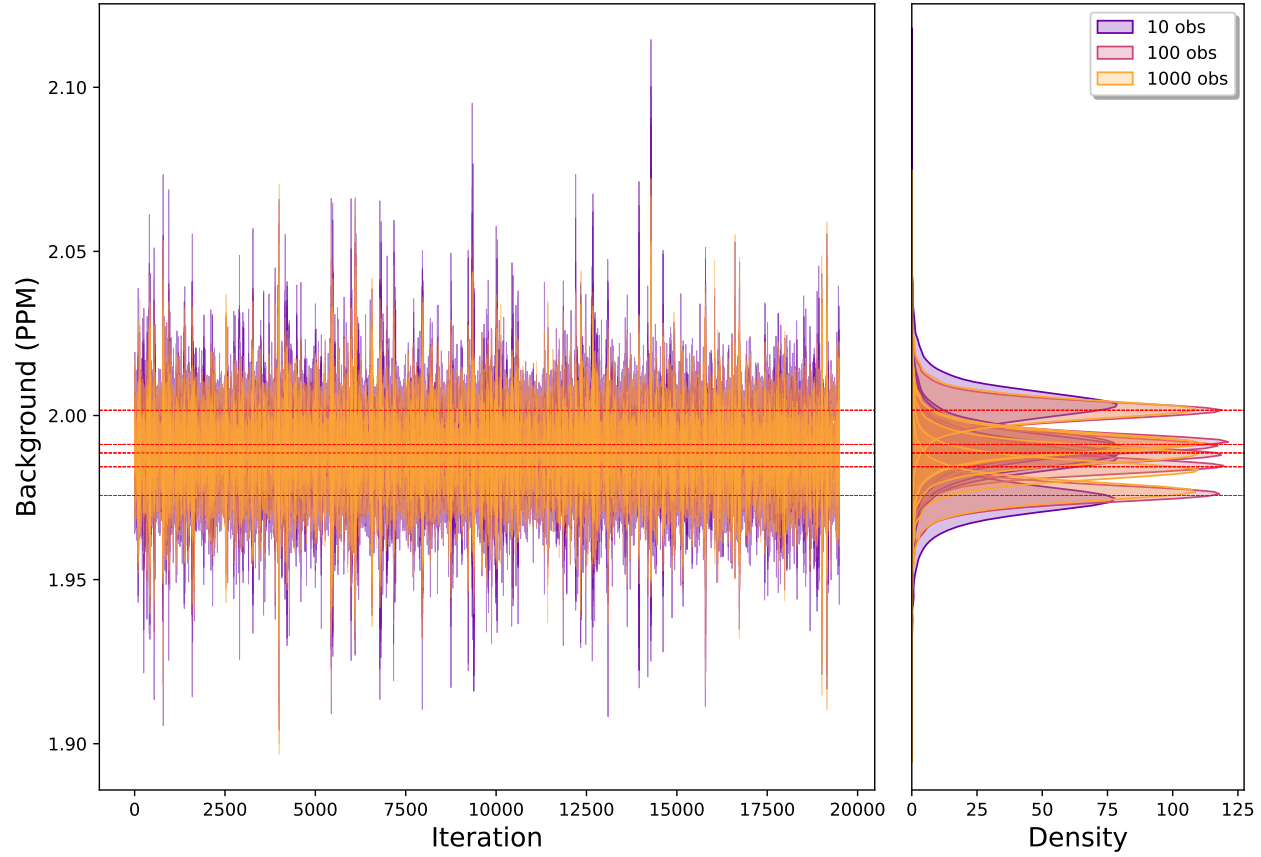


Figure 35: Background concentration estimation chains for varying number of observation per sensor.

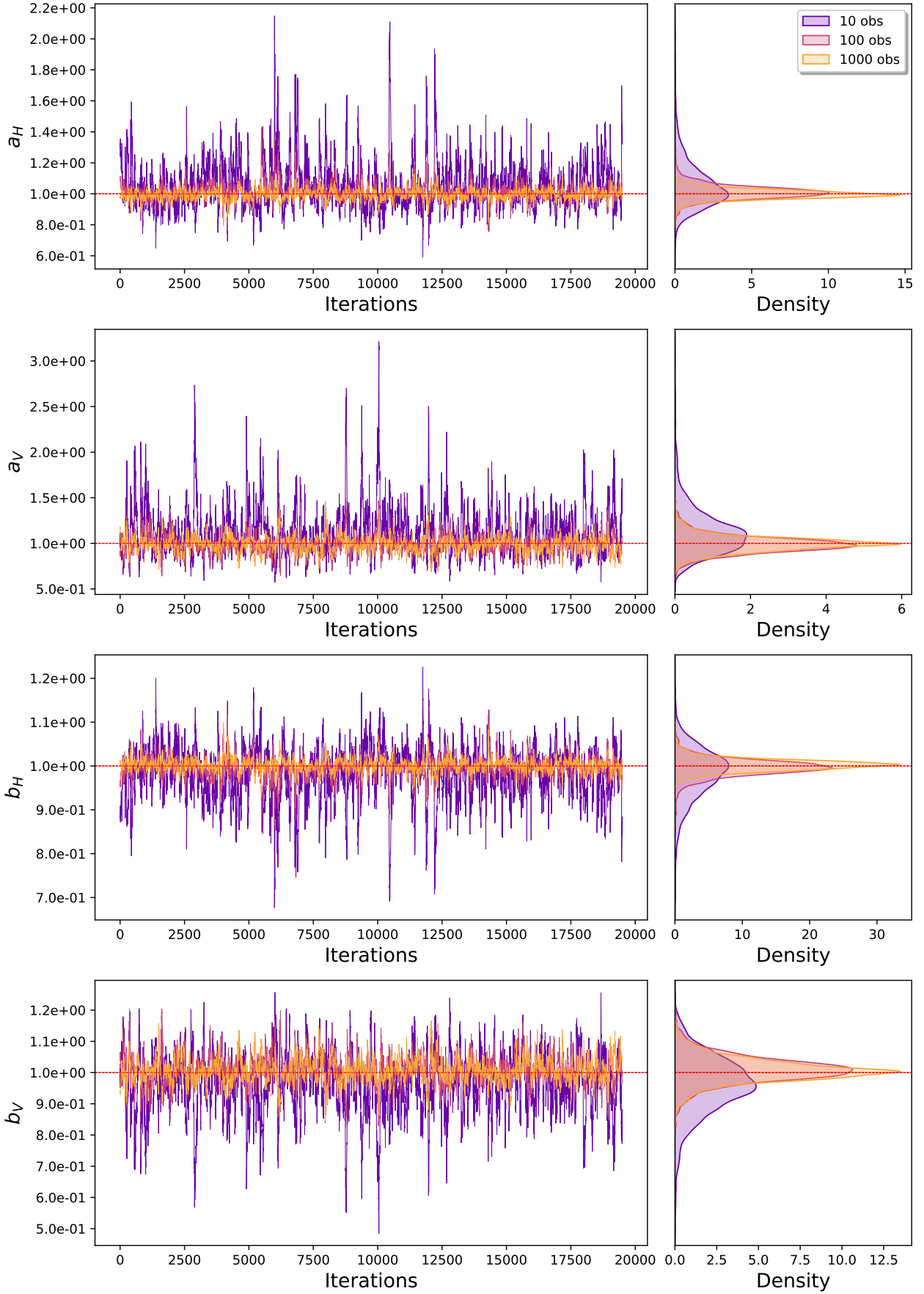


Figure 36: Diffusion parameter estimation chains for varying number of observation per sensor.

1.6 Varying the Sensor Layout

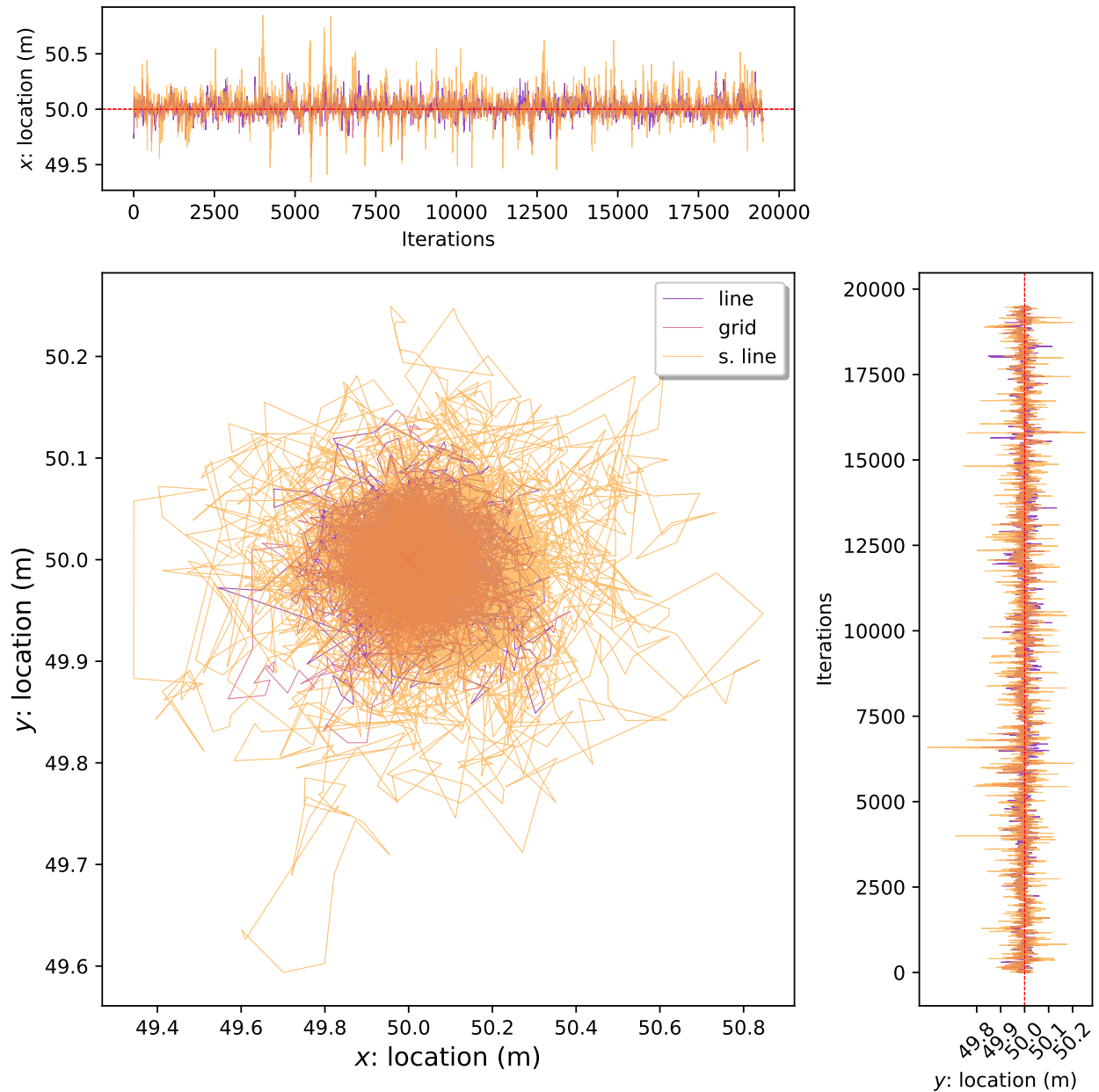


Figure 37: Source location estimation chains for varying the sensor layout. **line**: a line of 36x1 sensors, **grid**: a 6x6 grid of sensors, and **s.line**: a line of 6x1 sensors.

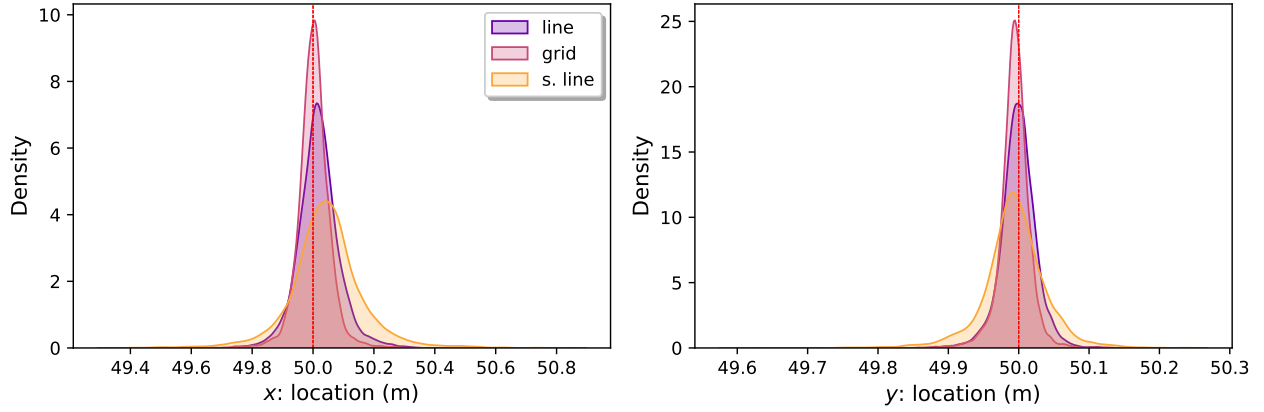


Figure 38: Source location estimation densities for varying the sensor layout. **line**: a line of 36x1 sensors, **grid**: a 6x6 grid of sensors, and **s.line**: a line of 6x1 sensors.

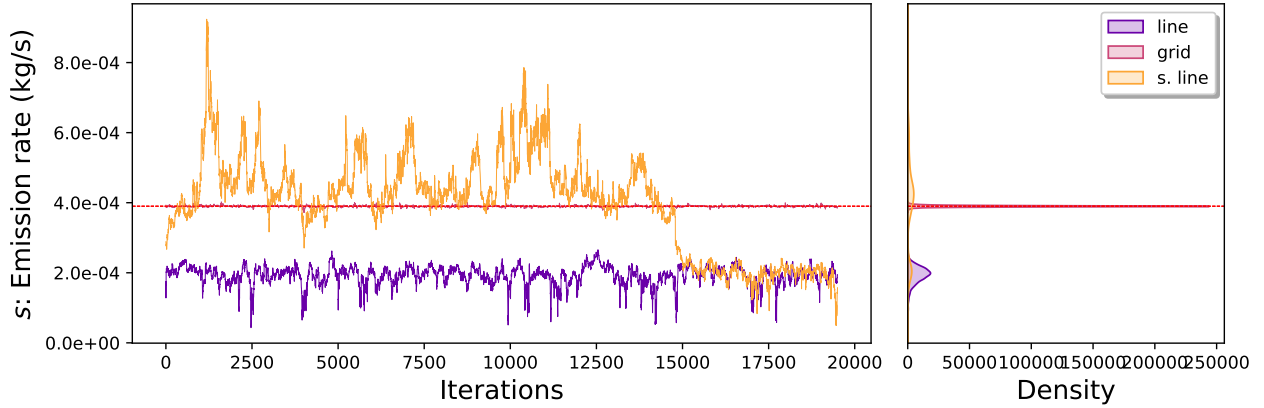


Figure 39: Source emission rate location estimation chains for varying the sensor layout. **line**: a line of 36x1 sensors, **grid**: a 6x6 grid of sensors, and **s.line**: a line of 6x1 sensors.

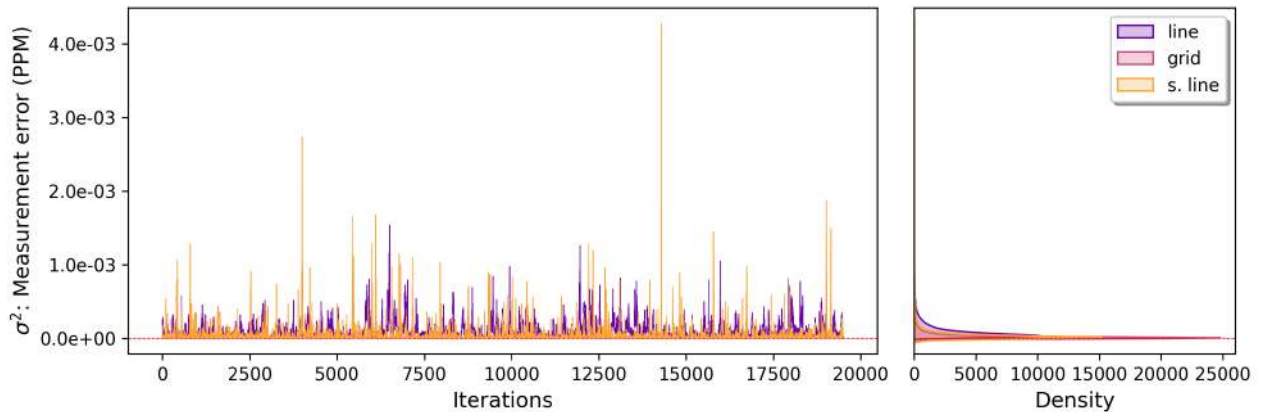


Figure 40: Sensor measurement error variance estimation chains for varying the sensor layout. **line**: a line of 36x1 sensors, **grid**: a 6x6 grid of sensors, and **s.line**: a line of 6x1 sensors.

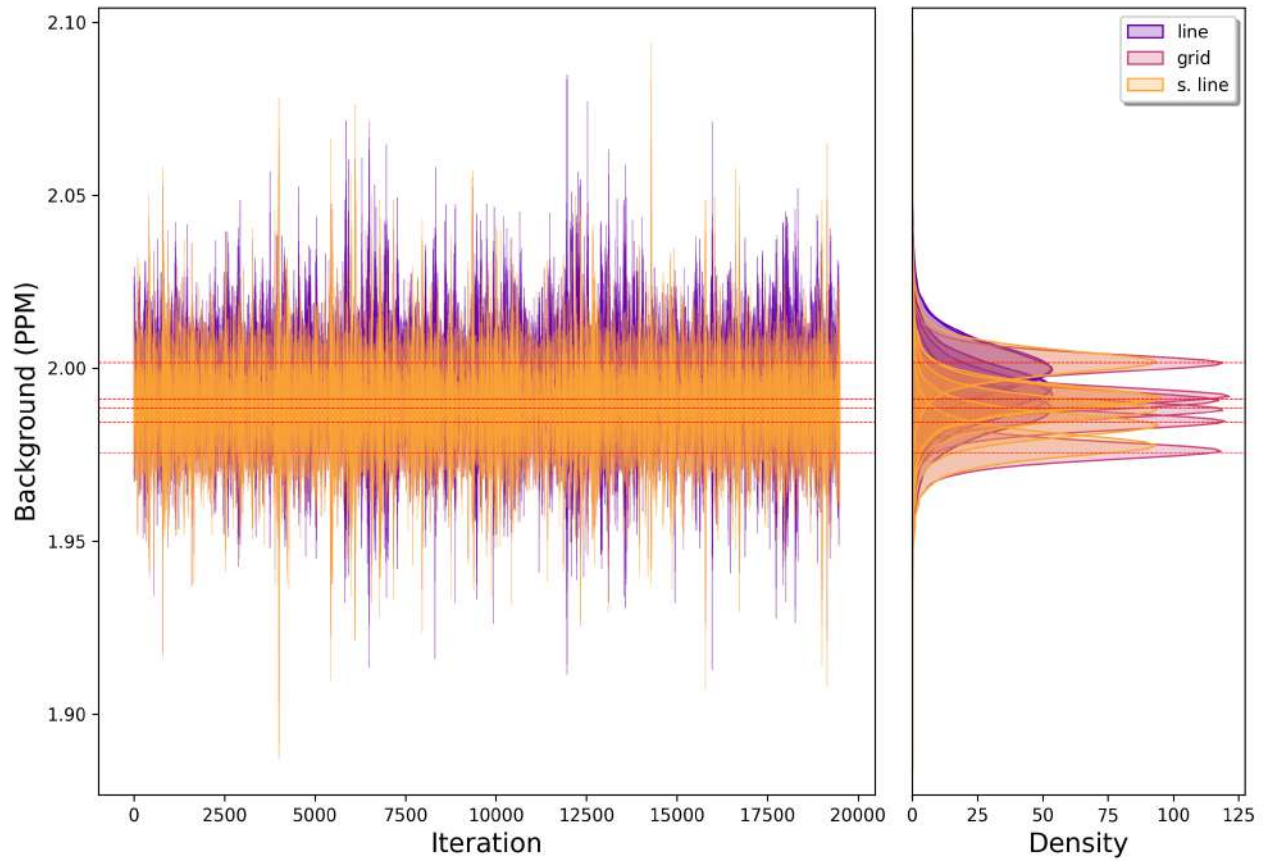


Figure 41: Background concentration estimation chains for varying the sensor layout. **line**: a line of 36x1 sensors, **grid**: a 6x6 grid of sensors, and **s.line**: a line of 6x1 sensors.

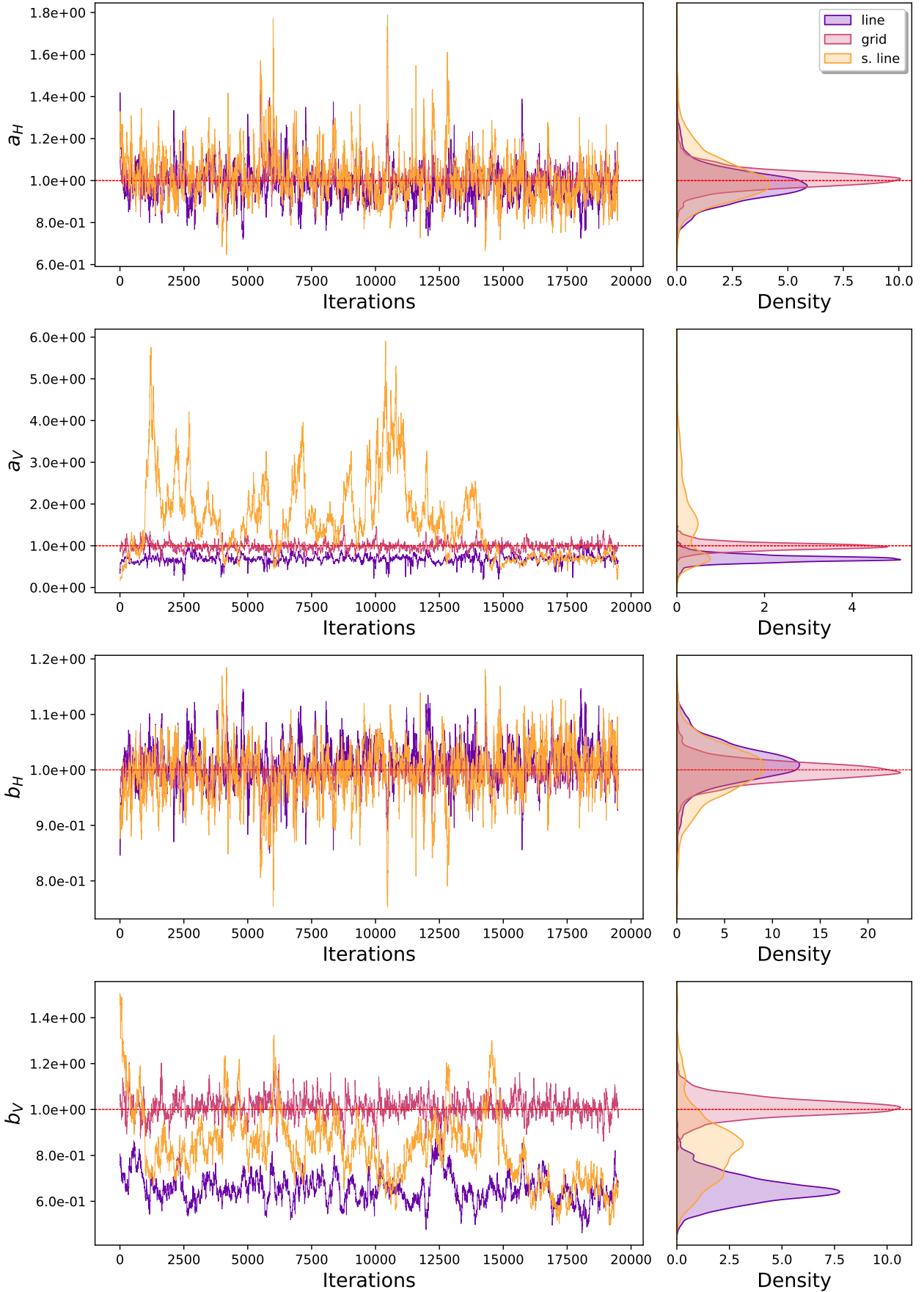


Figure 42: Diffusion parameter estimation chains for varying the sensor layout. **line**: a line of 36x1 sensors, **grid**: a 6x6 grid of sensors, and **s.line**: a line of 6x1 sensors.

In-depth simulation: Here we estimated the parameters for a range of sensor layouts and different numbers of sensors: 4, 9, 16, and 36. We have grid formations: 2×2 , 3×3 , 4×4 and 6×6 and line formations: 4×1 , 9×1 , 16×1 and 36×1 . The loss of vertical coverage in the line formations (equally spaced sensors at fixed height impacts the ability to accurately estimate the vertical dispersion parameters correctly and impacts the emission rate estimation. To explain the data, this increases the measurement error variance. However, grid formations show greater robustness even with a low number of sensors.

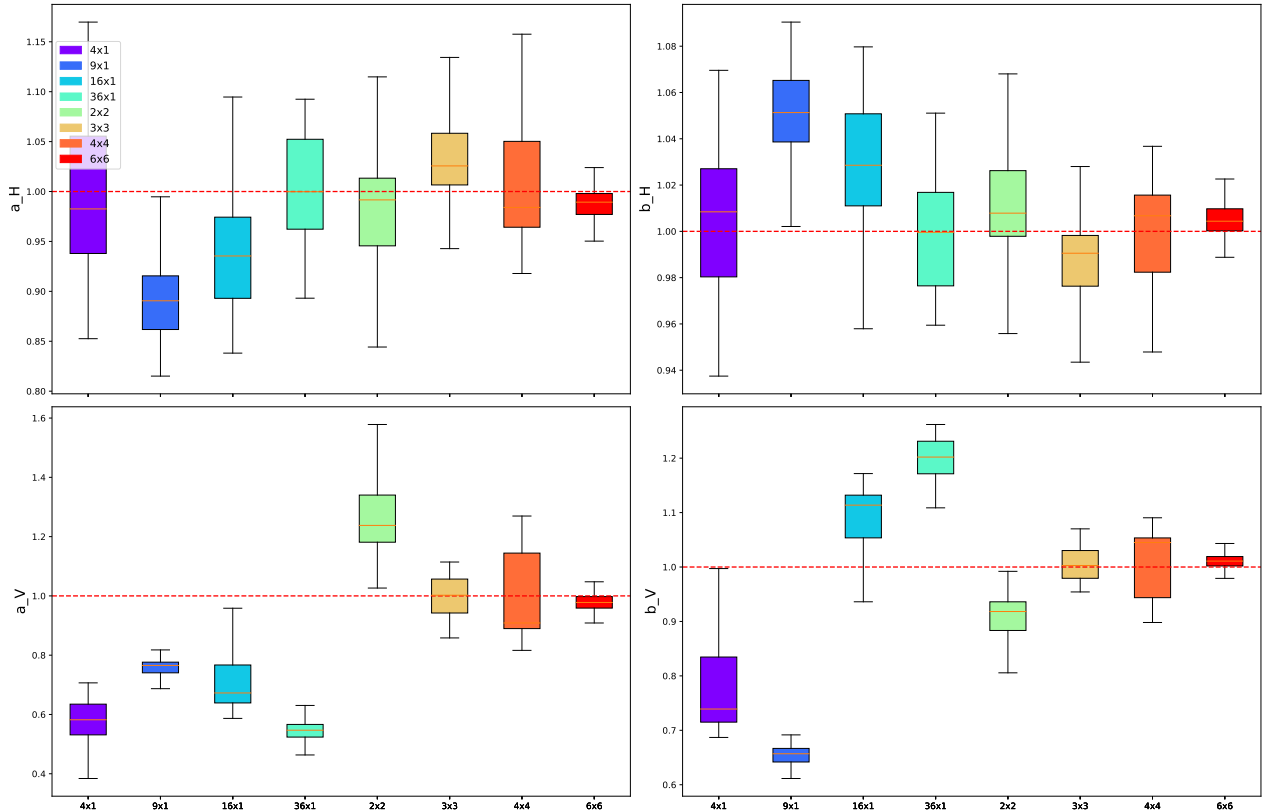


Figure 43: Dispersion parameters estimation for varying the sensor layout. We are comparing line layouts and grid layouts for different number of sensors.

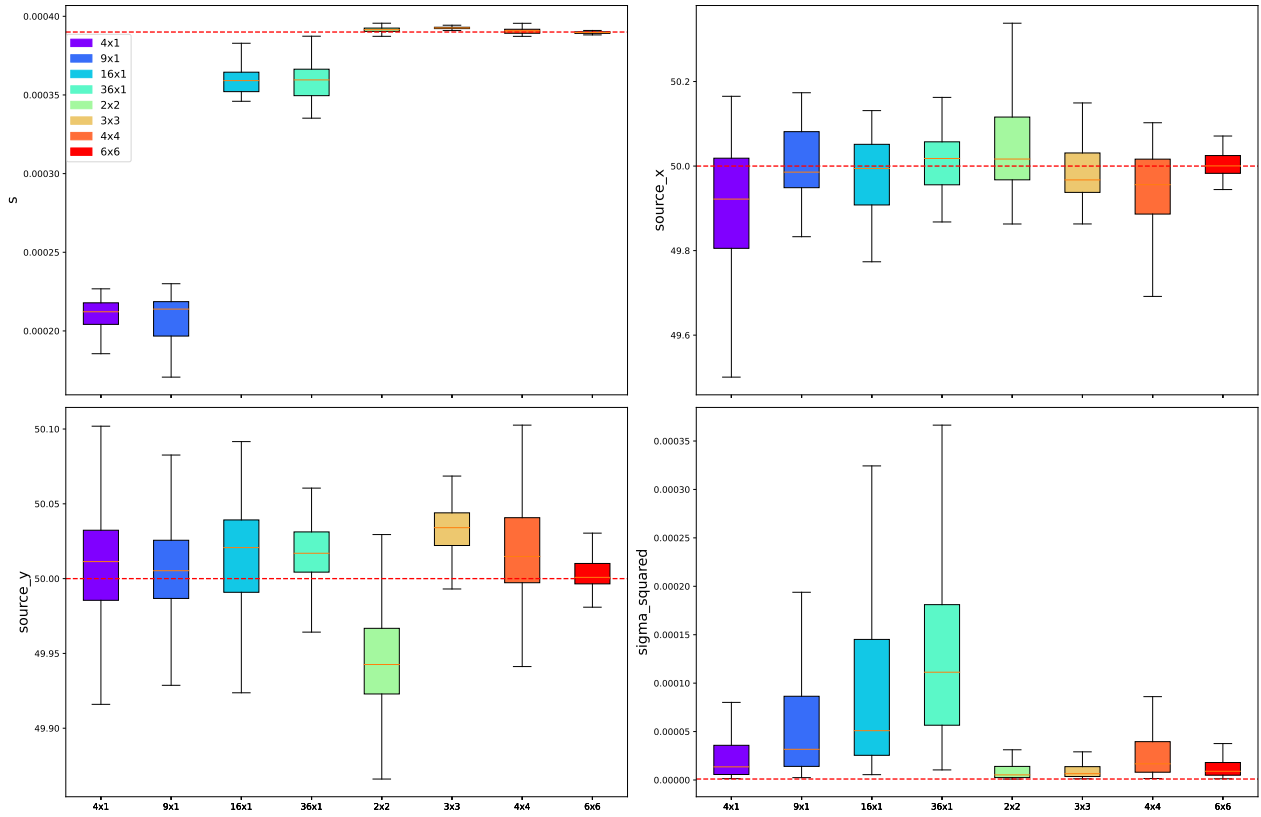


Figure 44: Source emission rate, location, and sensor measurement error variance estimation for varying the sensor layout. We are comparing line layouts and grid layouts for different number of sensors.

2 Chilbolton Dataset

2.1 Data Processing

The GitHub repository available at [https://github.com/NewmanTHP/Probabilistic-Inversion-Modeling-of-tree/master/Code/Chilbolton_Case_Study%20\(Section%205%2B%20SM.B%202\)/Data%20Processing%20\(SM.B%202.1\)](https://github.com/NewmanTHP/Probabilistic-Inversion-Modeling-of-tree/master/Code/Chilbolton_Case_Study%20(Section%205%2B%20SM.B%202)/Data%20Processing%20(SM.B%202.1)) contains jupyter notebooks detailing how the raw data was processed.

2.2 SMITH Scheme

The SMITH scheme used to fix the wind sigma parameters in the Gaussian plume model has the following parametric form:

$$\sigma_H = a_H \delta_R^{b_H},$$

$$\sigma_V = a_V \delta_R^{b_V},$$

where $\delta_R \in \mathbb{R}^+$ is the downwind distance. The dispersion parameters a_H, b_H, a_V, b_V are chosen based on the local atmospheric stability class (ASC) at the time the data was collected. Once the ASC is determined the dispersion parameters can be chosen using Table 1 from Hanna et al. [1982].

Table 1: Briggs ASC-based dispersion parameter table

ASC	a_H	b_H	a_V	b_V
B	0.4	0.91	0.41	0.91
C	0.36	0.86	0.33	0.86
D	0.32	0.78	0.22	0.78

2.3 Briggs Scheme

The Briggs scheme used to fix the wind sigma parameters in the Gaussian plume model has the following parametric form:

$$\sigma_H = a \delta_R (1 + 0.0001 \delta_R)^{-0.5},$$

$$\sigma_V = \begin{cases} b \delta_R & \text{if ASC is A or B} \\ b \delta_R (1 + c \delta_R)^d & \text{if ASC is C, D, E or, F.} \end{cases}$$

where $\delta_R \in \mathbb{R}^+$ is the downwind distance. The dispersion parameters a, b, c, d are chosen based on the local atmospheric stability class (ASC) at the time the data was collected. Once the ASC is determined the dispersion parameters can be chosen using Table 2 from Hanna et al. [1982].

Table 2: Briggs ASC-based dispersion parameter table for open country conditions

ASC	<i>a</i>	<i>b</i>	<i>c</i>	<i>d</i>
A	0.22	0.20	0	0
B	0.16	0.12	0	0
C	0.11	0.08	0.0002	-0.5
D	0.08	0.06	0.0015	-0.5
E	0.06	0.03	0.0003	-1
F	0.04	0.016	0.0003	-1

2.4 Atmospheric Stability Class Determination

Pasquill's ASC system is determined by wind speed and net solar radiation index. The following classification table is drawn:

Table 3: Pasquill ASC table

Wind Speed (m/s)	Daytime incoming solar radiation		
	Strong	Moderate	Slight
<2	A	A-B	B
2-3	A-B	B	C
3-5	B	B-C	C
5-6	C	C-D	D
>6	C	D	D

where strong $> 700 \text{Wm}^2$, moderate $350\text{-}700 \text{Wm}^2$, and slight $< 350 \text{Wm}^2$ [Seinfeld and Pandis, 2016]. During the Chilbolton experiments, wind speeds were between 1 and 5 m/s. There is no other measured information about the weather conditions at the time of the release. Furthermore, the UK Met Office data for the closest meteorological observation stations do not cover the period of interest. The only available information regarding the radiation index is a picture of the release site taken during the experiments. A light grey sky is visible from which we assumed the radiation index was moderate. Therefore, using table 3 we would expect the Chilbolton experiments to have taken place under ASC B.

To overcome the lack of evidence needed to confidently determine the ASC, we performed an exploratory data analysis to identify the ASC. Instead of selecting a single ASC using the poor meteorological data available, we compared Smith and Briggs-based model predictions of spatial gas concentration measurements to the real data. This was done by computing the average CH₄ measurements observed by each beam for a carefully chosen subset of data points which we call a *slice*. The subset is chosen as to contain observations where the wind direction always intersects some of the beams. This ensures that for some beams the average CH₄ measurement is calculated using only observations where the plume is crossing their path. Then for each Smith and Briggs ASC wind sigma parametrization, we predicted the corresponding averaged CH₄ beam measurements, this is possible because we know the true source location and emission rate. Finally, we plot the CH₄ measurements against the downwind distance for the intersection points between the beams and the averaged wind direction line starting from the source location (as illustrated in Figure 45, 47, 49, 51, 53, and 55. Figure 46, 48, 50, 52, 54, and 56, shows the results for both Source 1 and Source 2, the local ASC could not be determined as the equally most accurate predictions came from the Smith B, Smith C, Briggs A, and Briggs B schemes.

This means that we cannot select a unique ASC for our inversion. Predictions made from est. Smith and est. Draxler's maximum a posteriori estimations of source emission rate and dispersion parameters were also added for comparison. These are represented by the dotted lines in Figure 46, 48, 50, 52, 54, and 56.

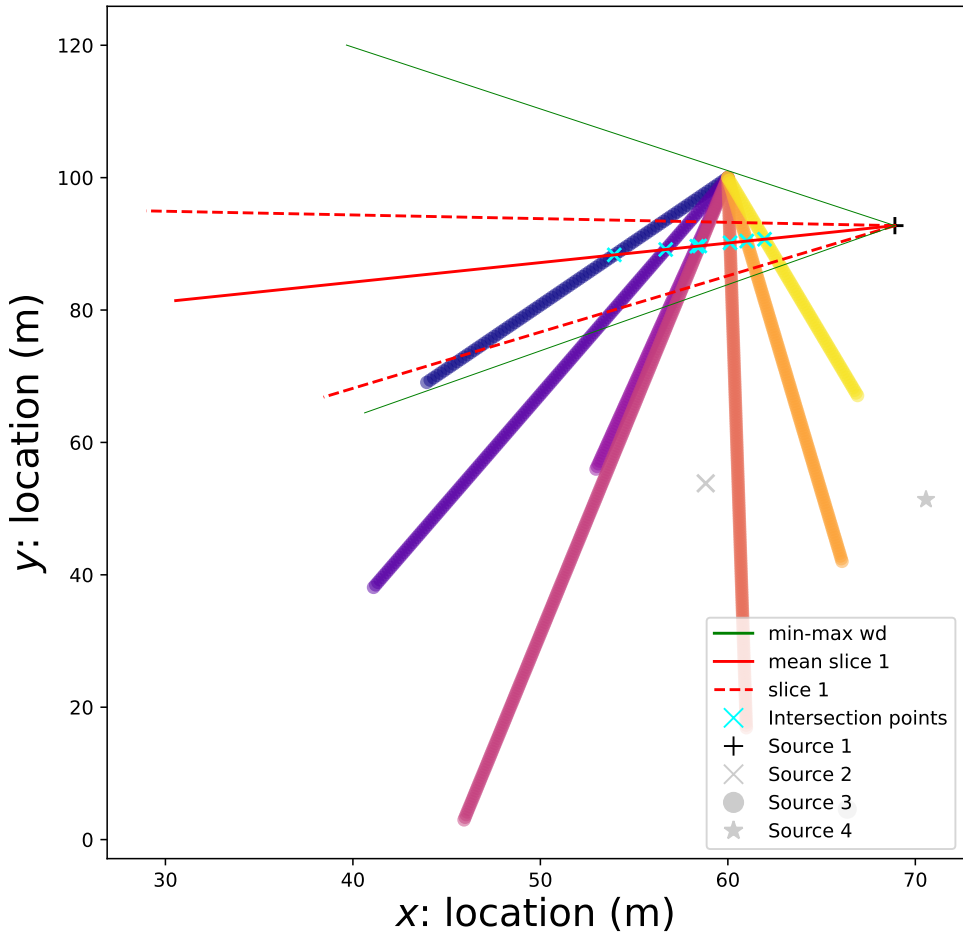


Figure 45: The dashed red lines represent the range of wind directions in slice 1 of Source 1 data and the straight red line is the average wind direction.

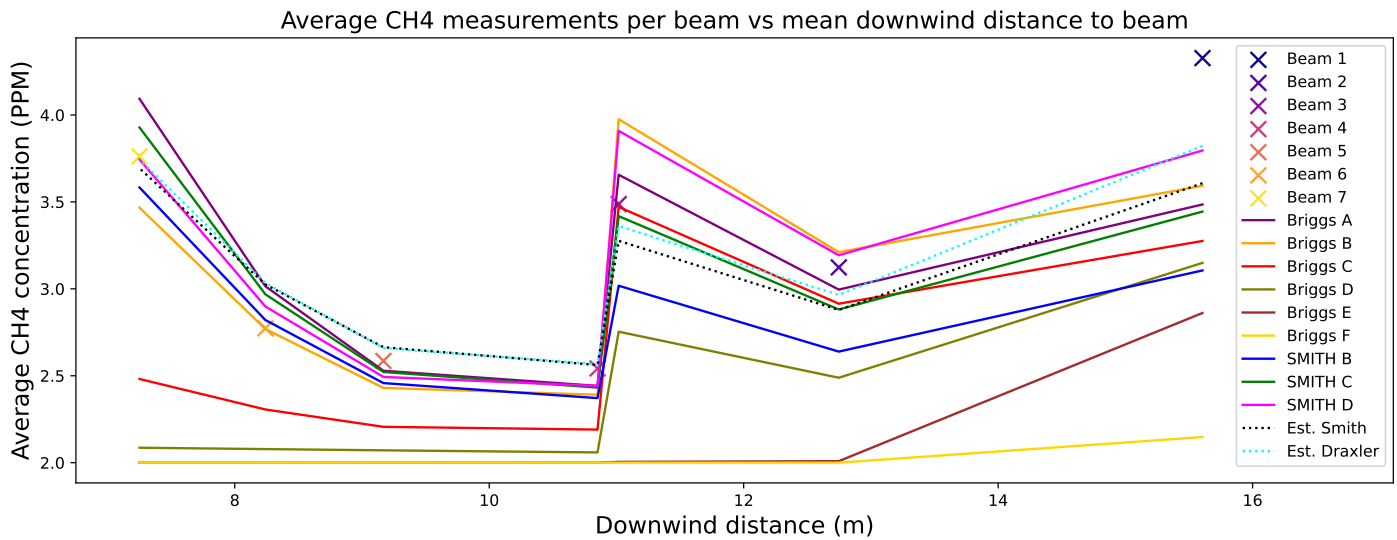


Figure 46: This plot shows the CH₄ measurements as a function of downwind distance and corresponding model predictions for slice 1 of Source 1 data.

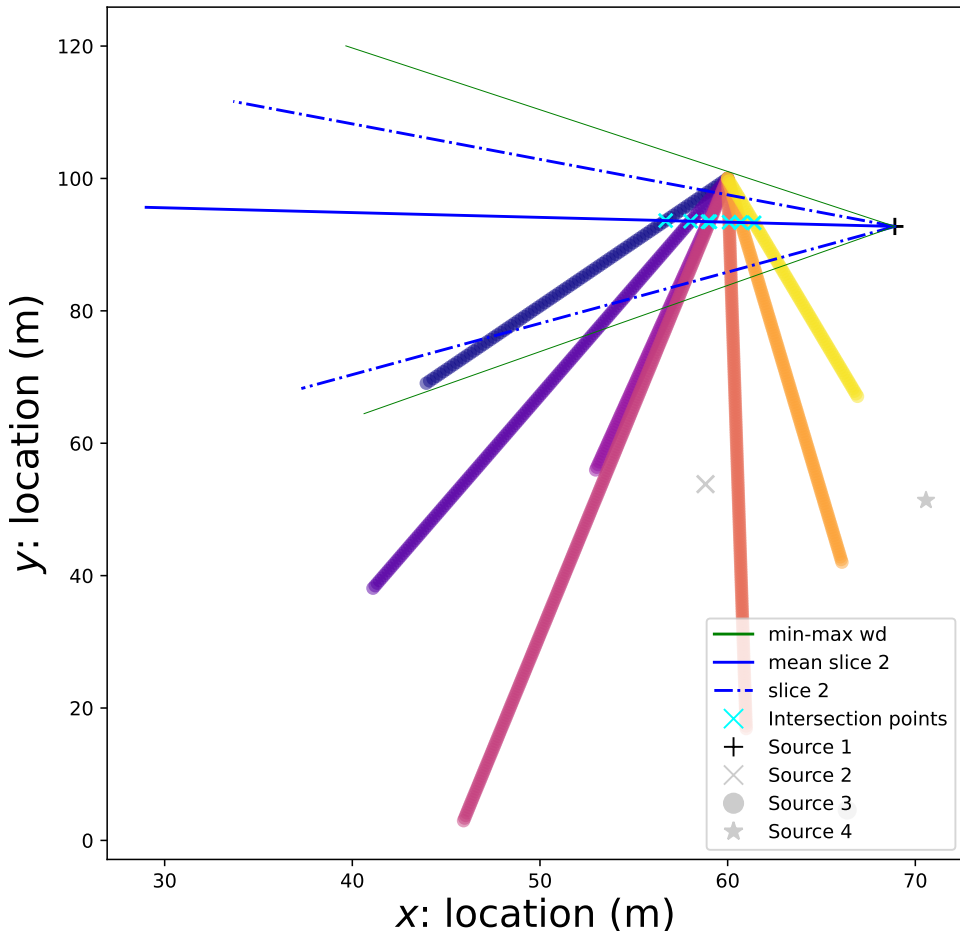


Figure 47: The dashed red lines represent the range of wind directions in slice 2 of Source 1 data and the straight red line is the average wind direction.

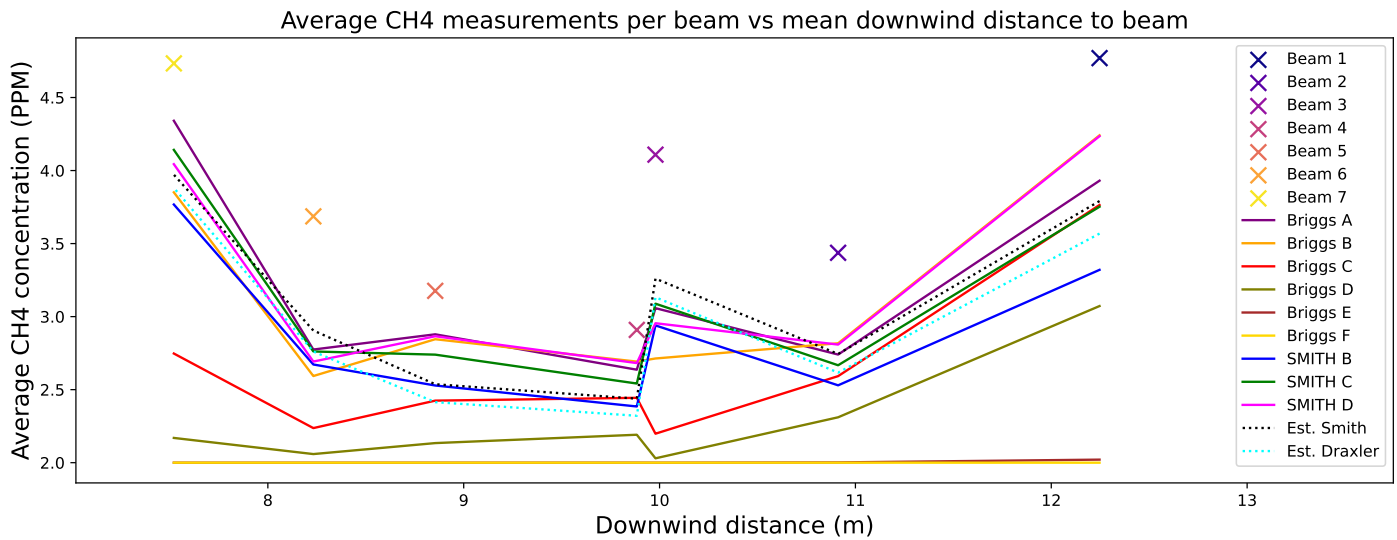


Figure 48: This plot shows the CH₄ measurements as a function of downwind distance and corresponding model predictions for slice 2 of Source 1 data.

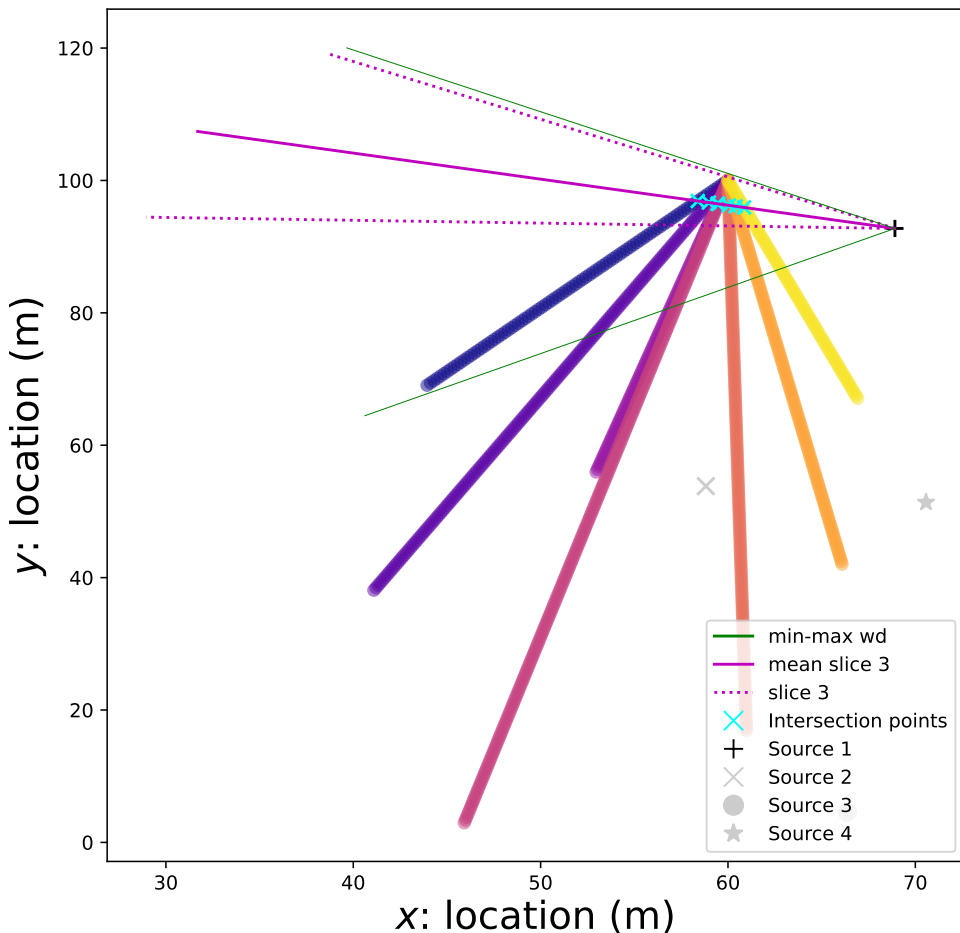


Figure 49: The dashed red lines represent the range of wind directions in slice 3 of Source 1 data and the straight red line is the average wind direction.

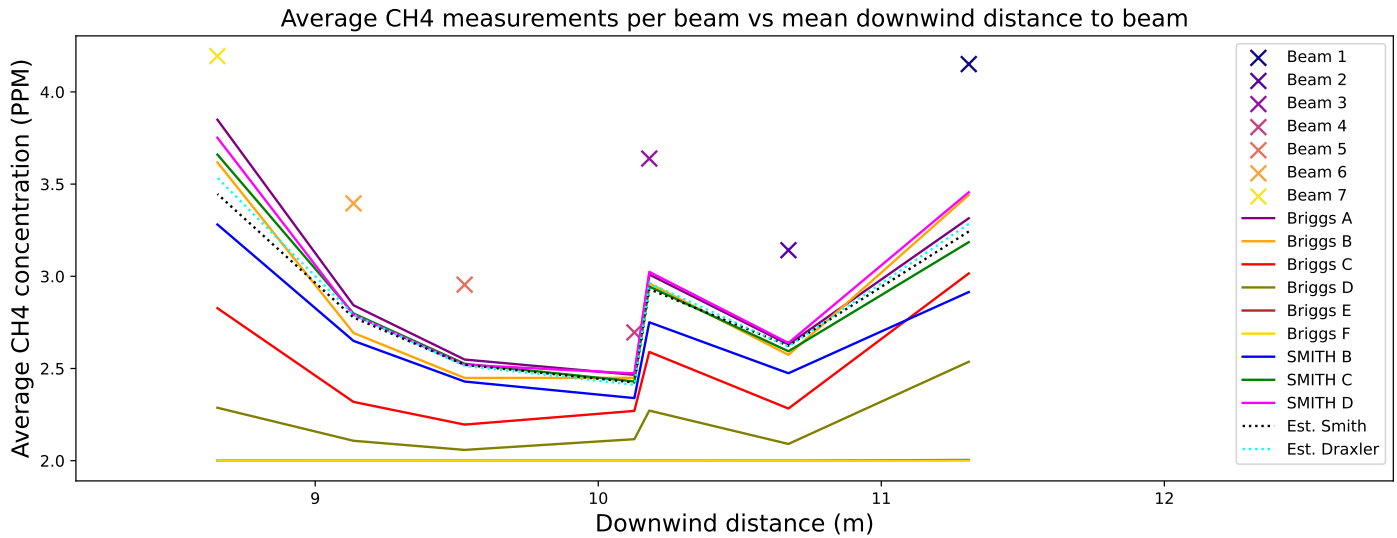


Figure 50: This plot shows the CH₄ measurements as a function of downwind distance and corresponding model predictions for slice 3 of Source 1 data.

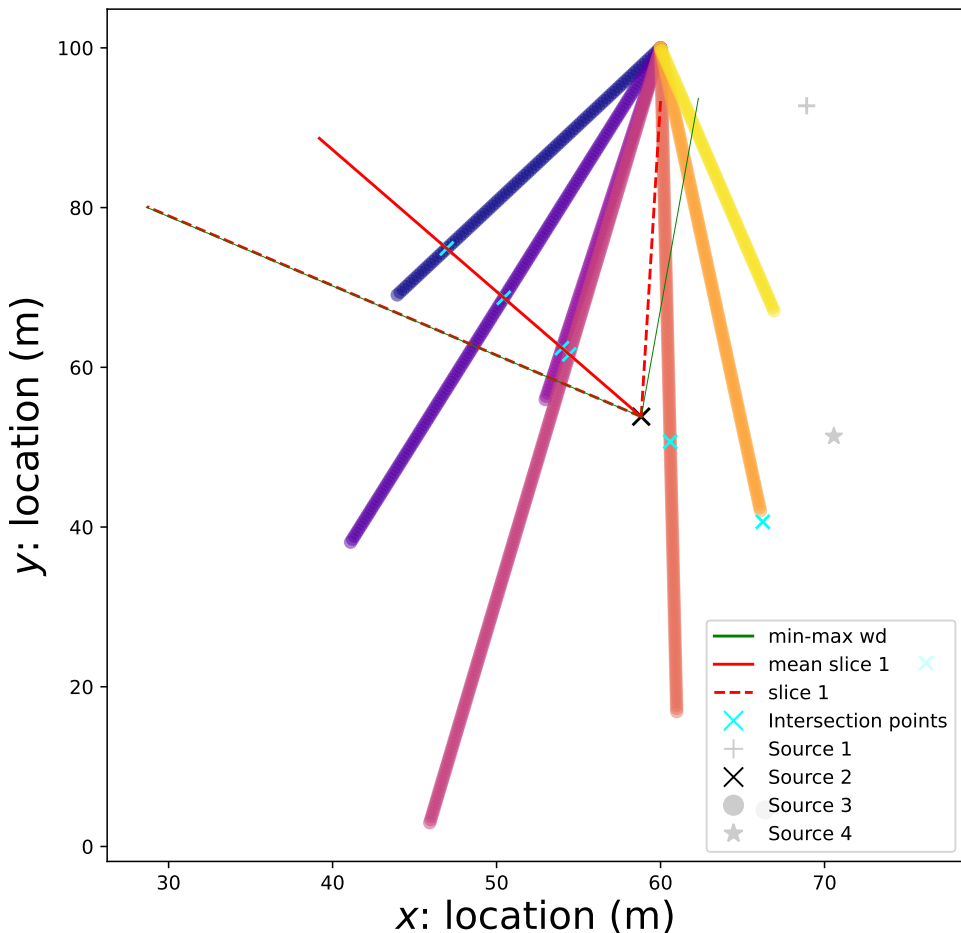


Figure 51: The dashed red lines represent the range of wind directions in slice 1 of Source 2 data and the straight red line is the average wind direction.

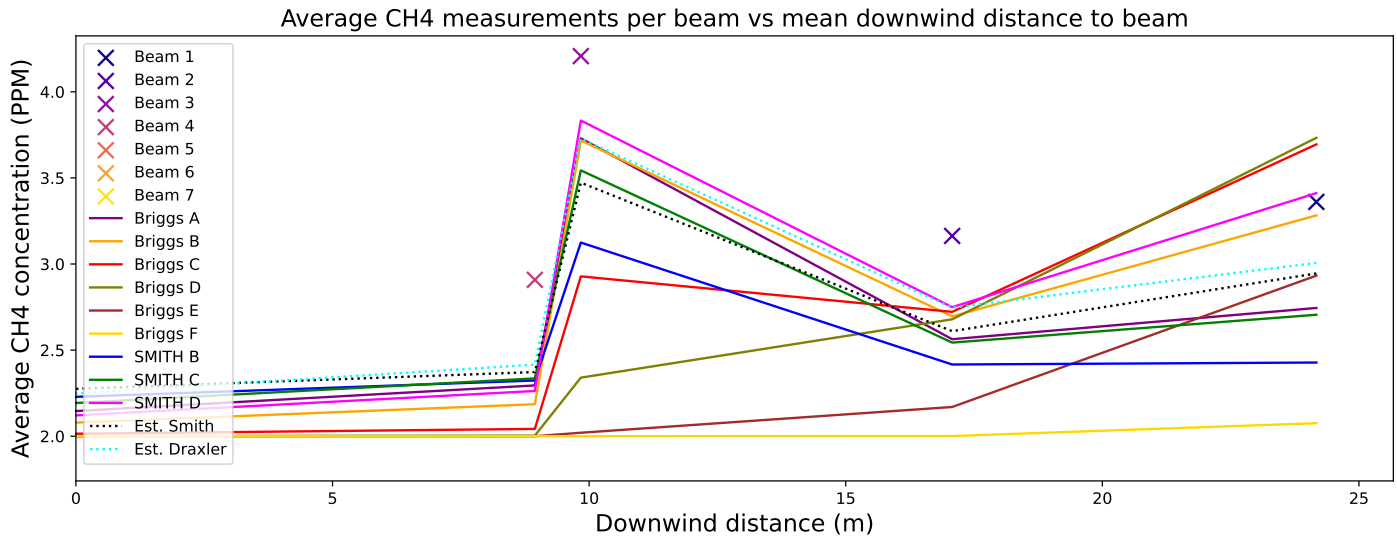


Figure 52: This plot shows the CH₄ measurements as a function of downwind distance and corresponding model predictions for slice 1 of Source 2.

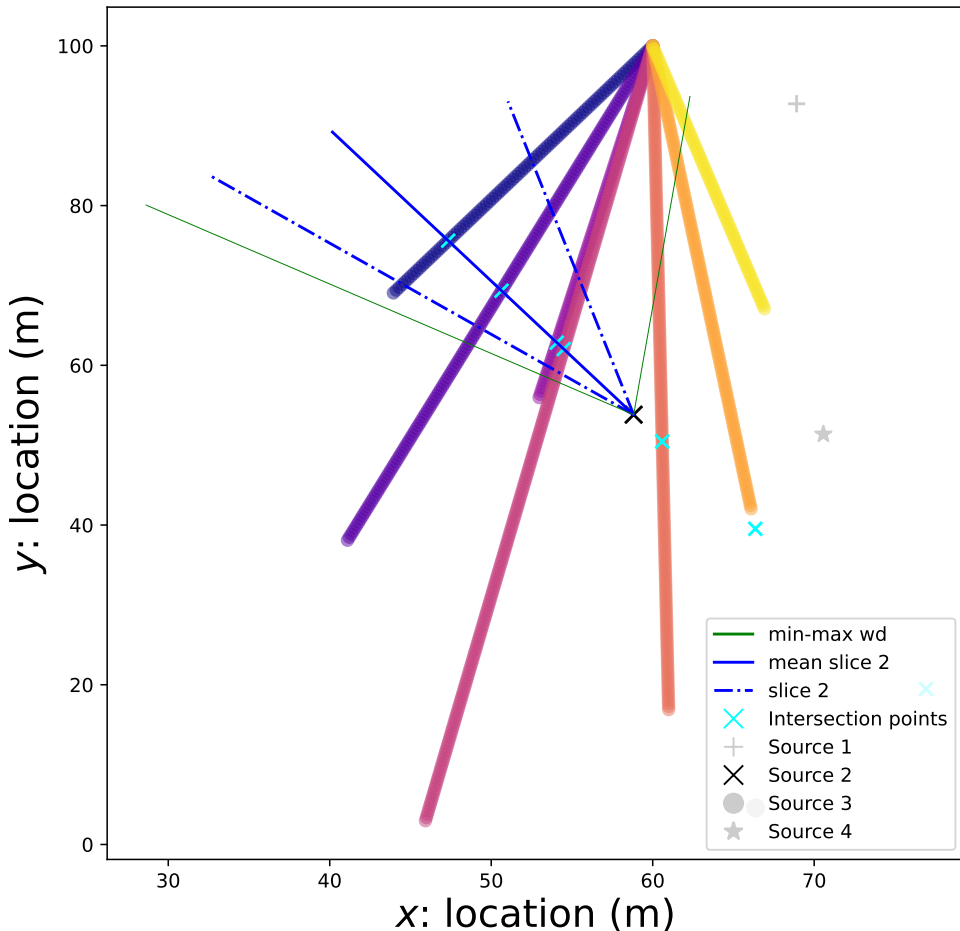


Figure 53: The dashed red lines represent the range of wind directions in slice 2 of Source 2 and the straight red line is the average wind direction.

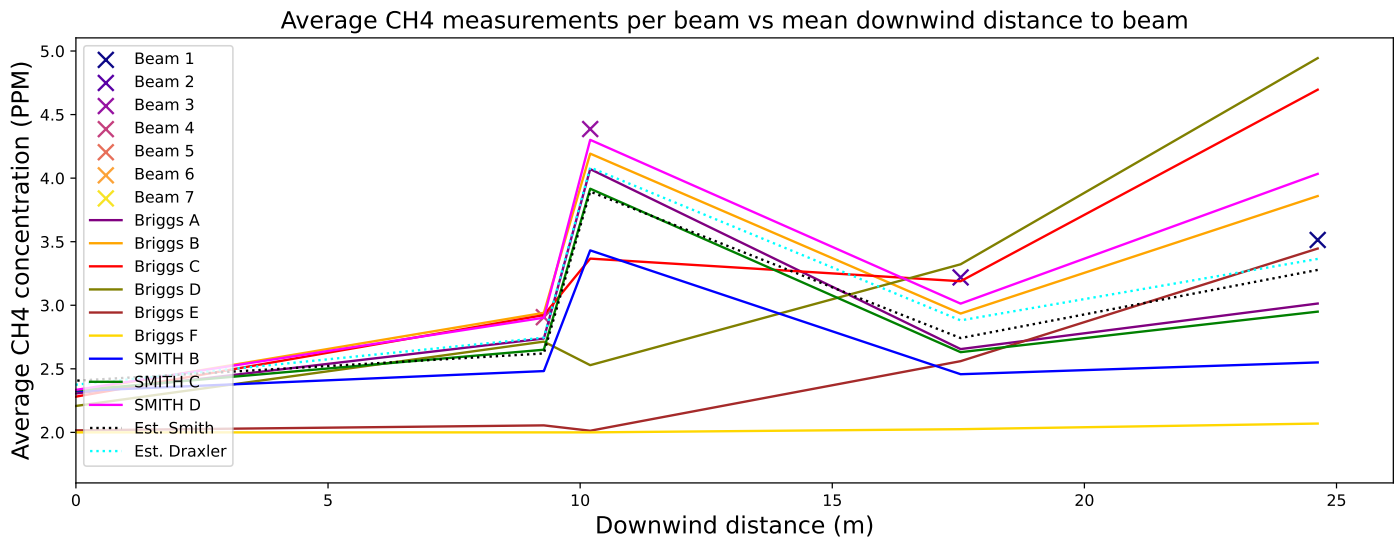


Figure 54: This plot shows the CH₄ measurements as a function of downwind distance and corresponding model predictions slice 2 of Source 2.

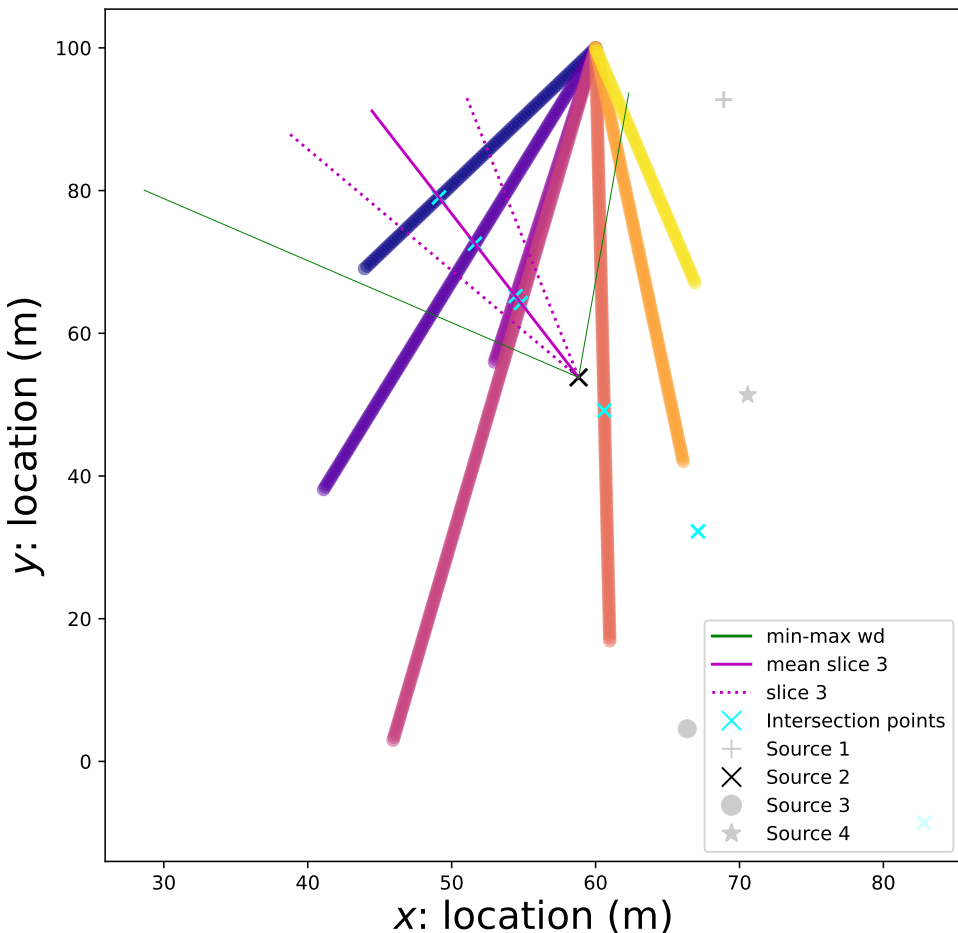


Figure 55: The dashed red lines represent the range of wind directions in slice 3 of Source 2 and the straight red line is the average wind direction.

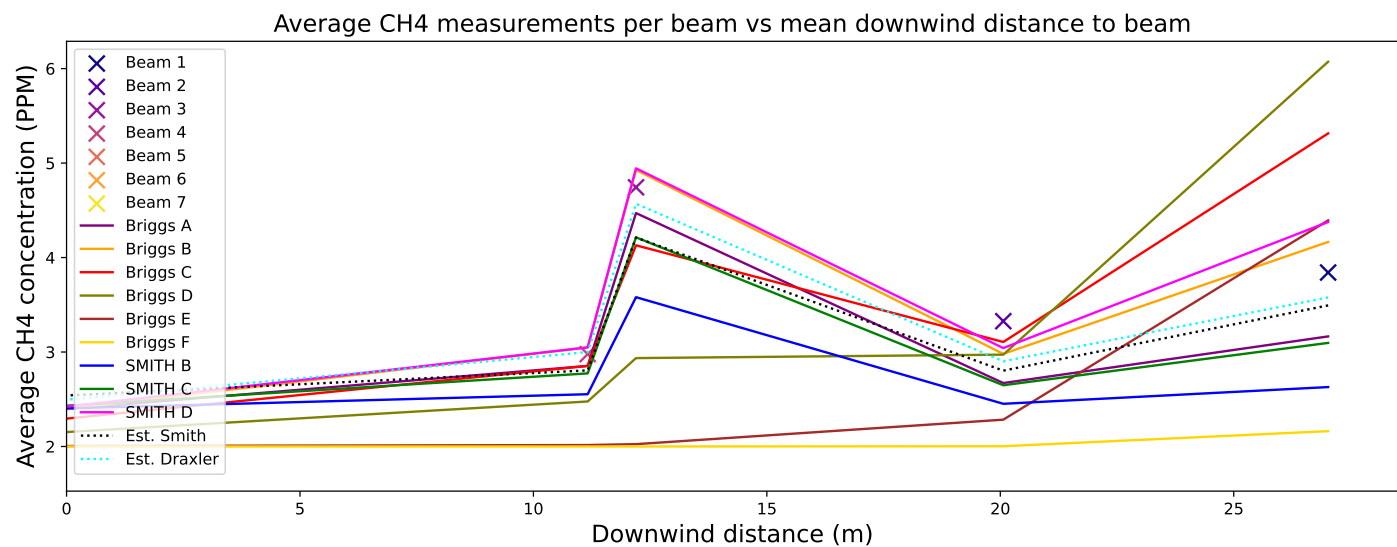


Figure 56: This plot shows the CH₄ measurements as a function of downwind distance and corresponding model predictions slice 3 of Source 2.

2.5 Chilbolton Source 1 Inversion

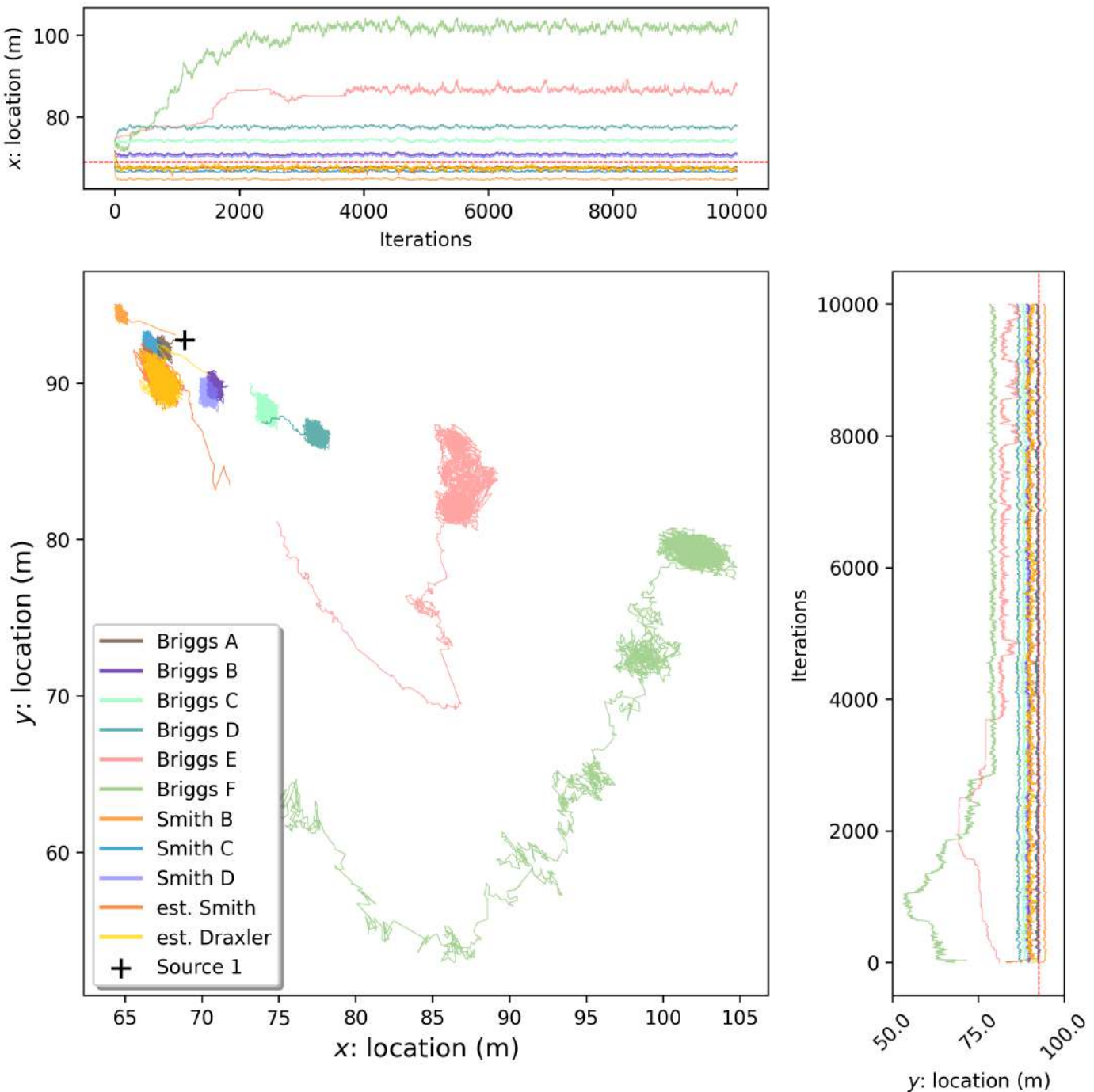


Figure 57: Source 1 location chains.

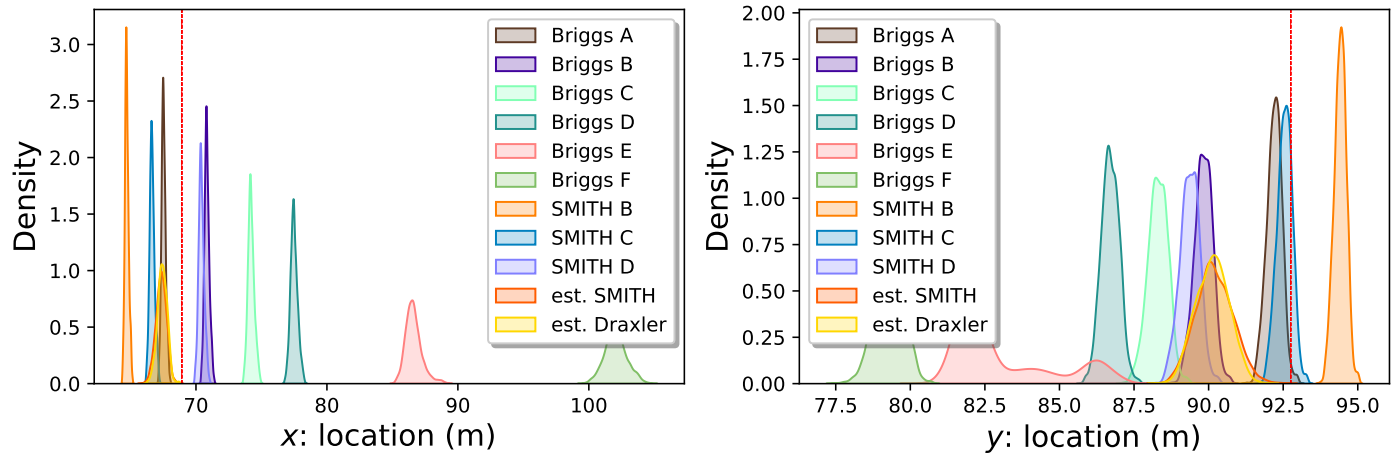


Figure 58: Source 1 location densities.

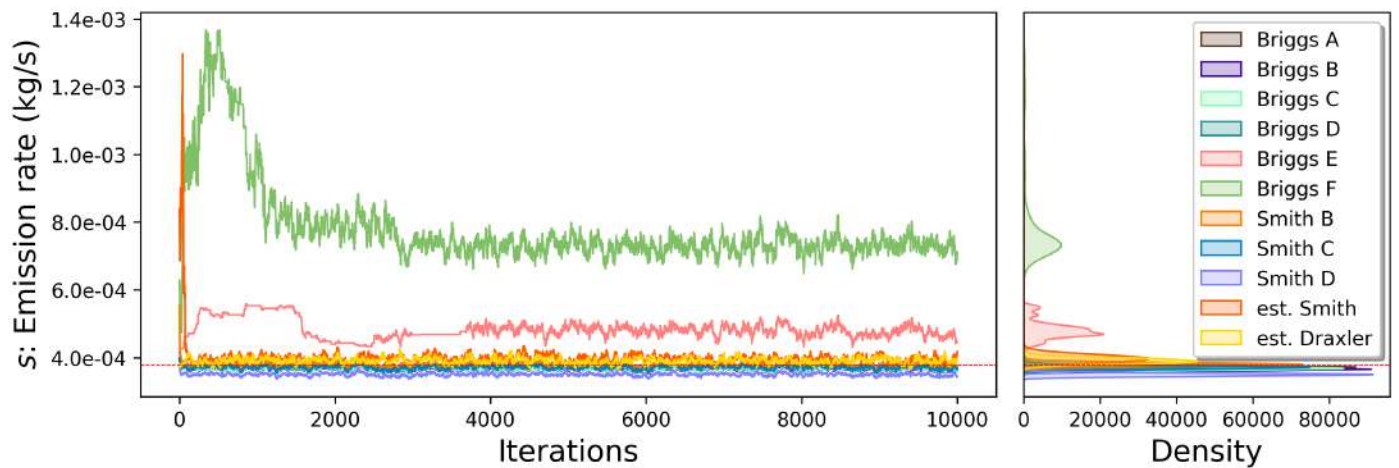


Figure 59: Source 1 emission rate.

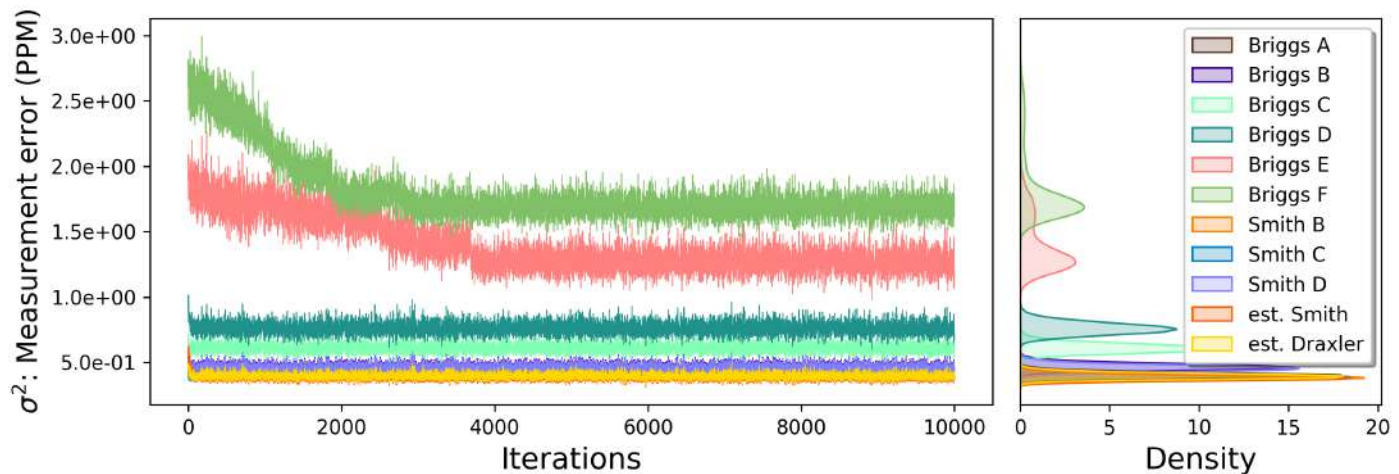


Figure 60: Source 1 measurement error variance.

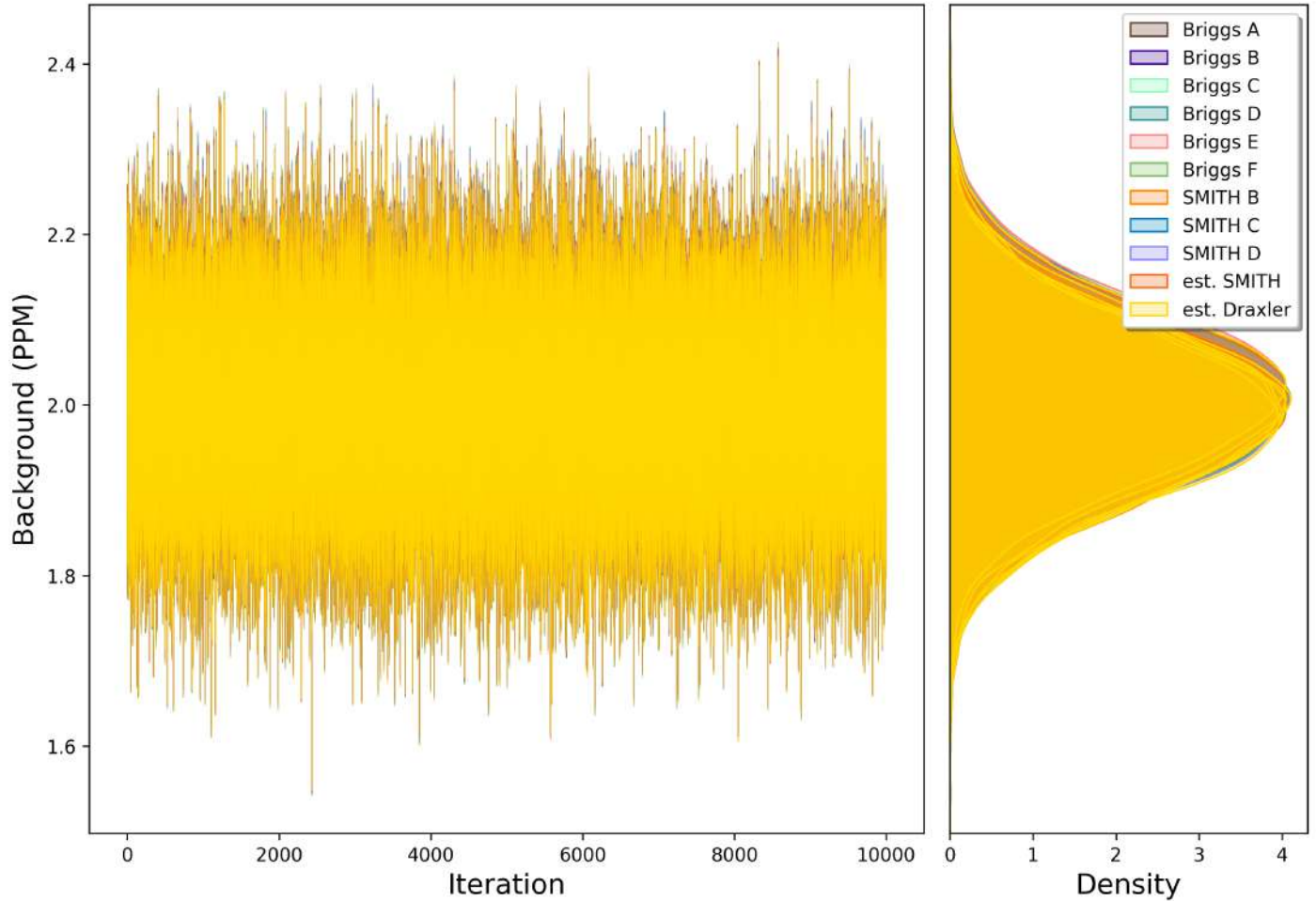
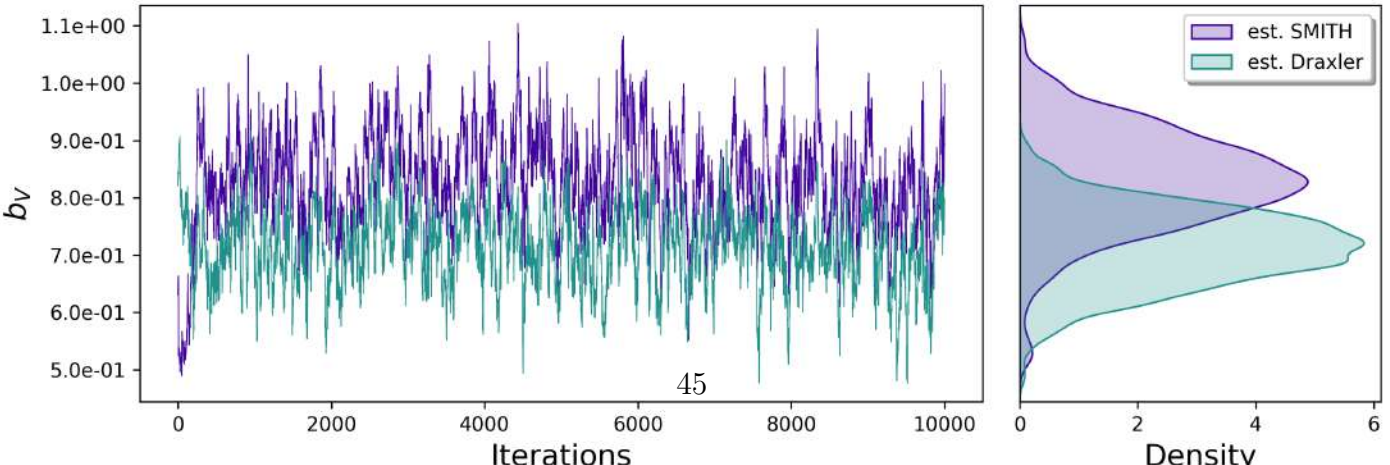
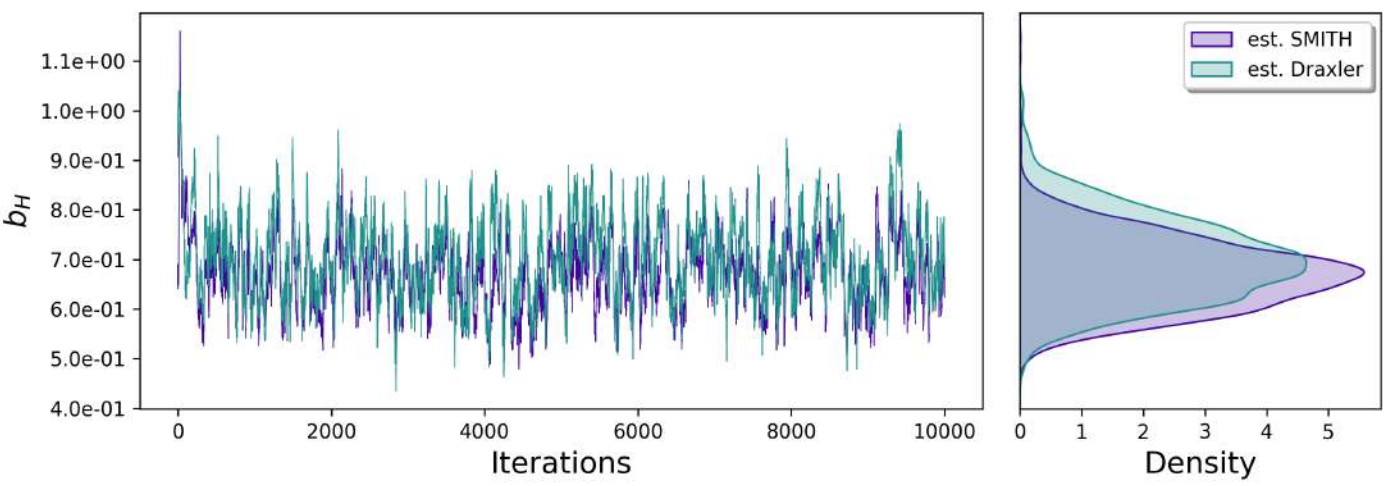
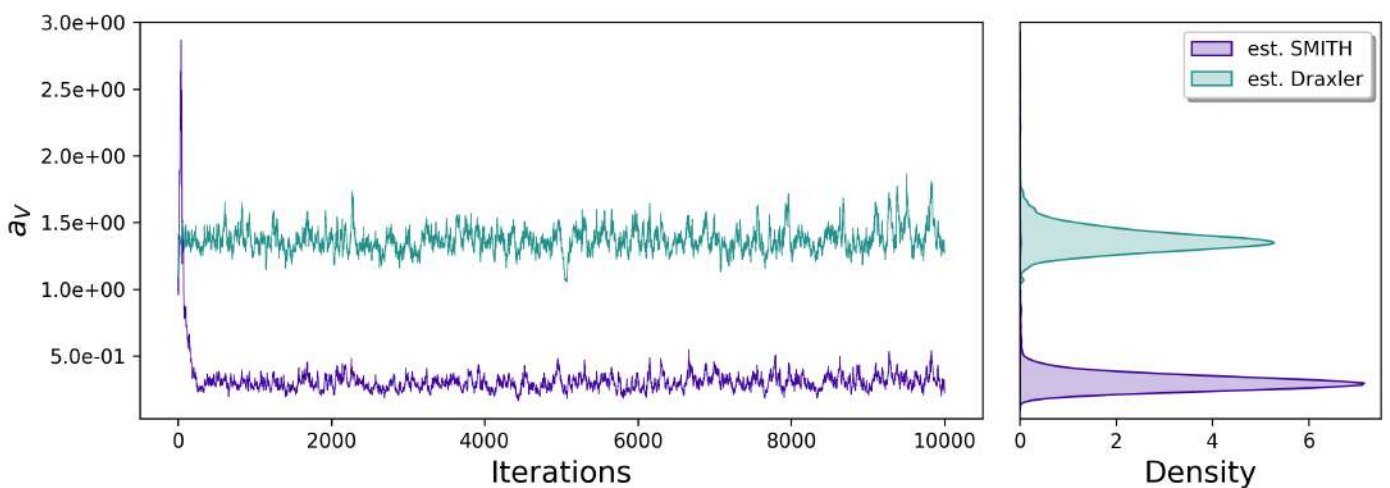
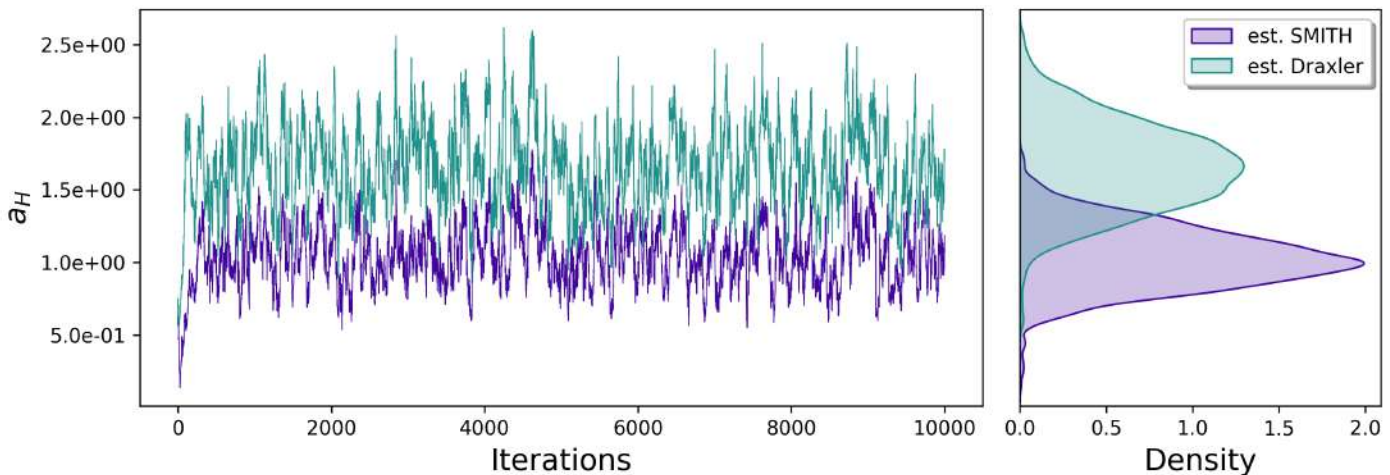


Figure 61: Source 1 background.



2.6 Chilbolton Source 2 Inversion

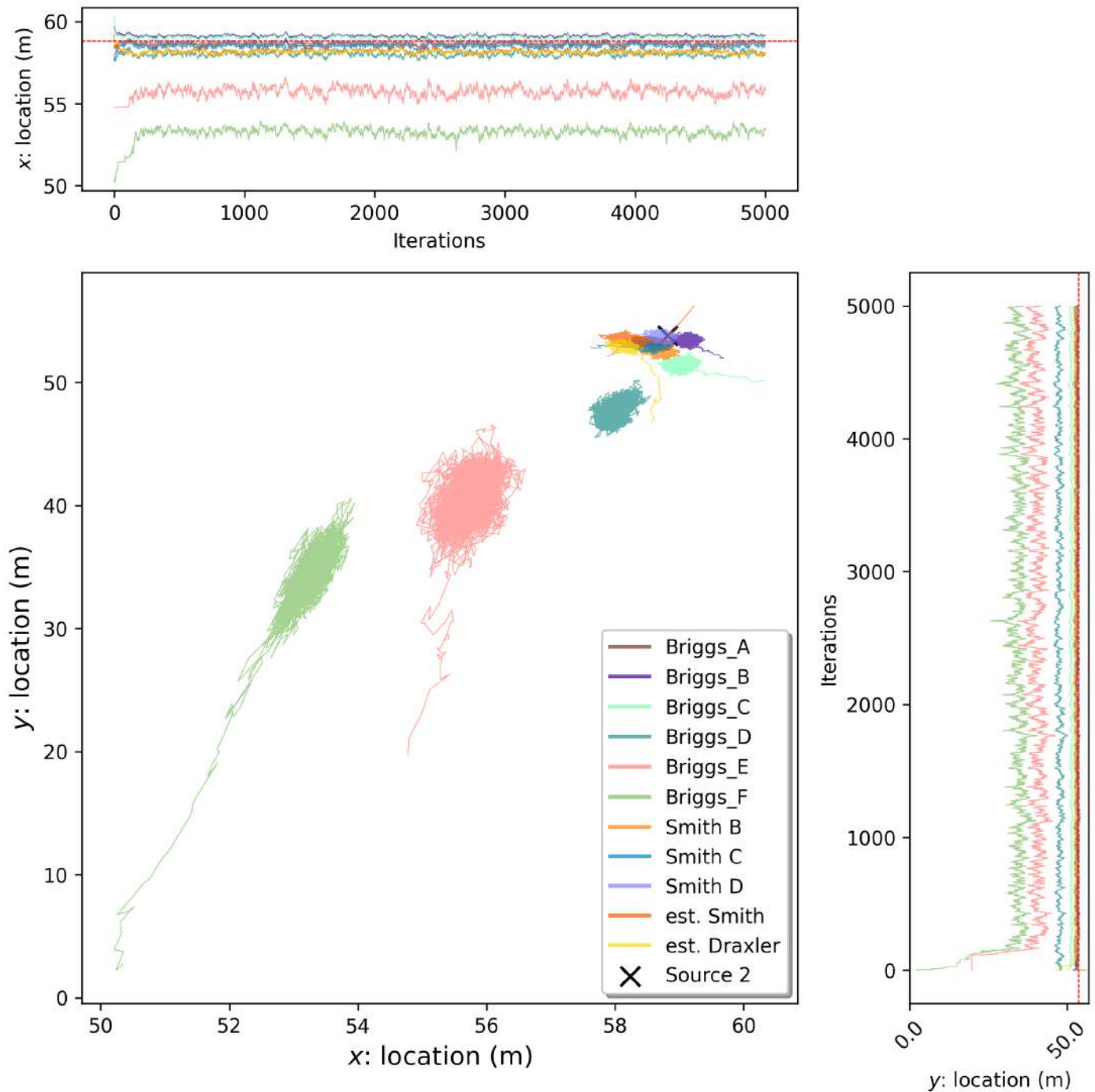


Figure 63: Source 2 location chains.

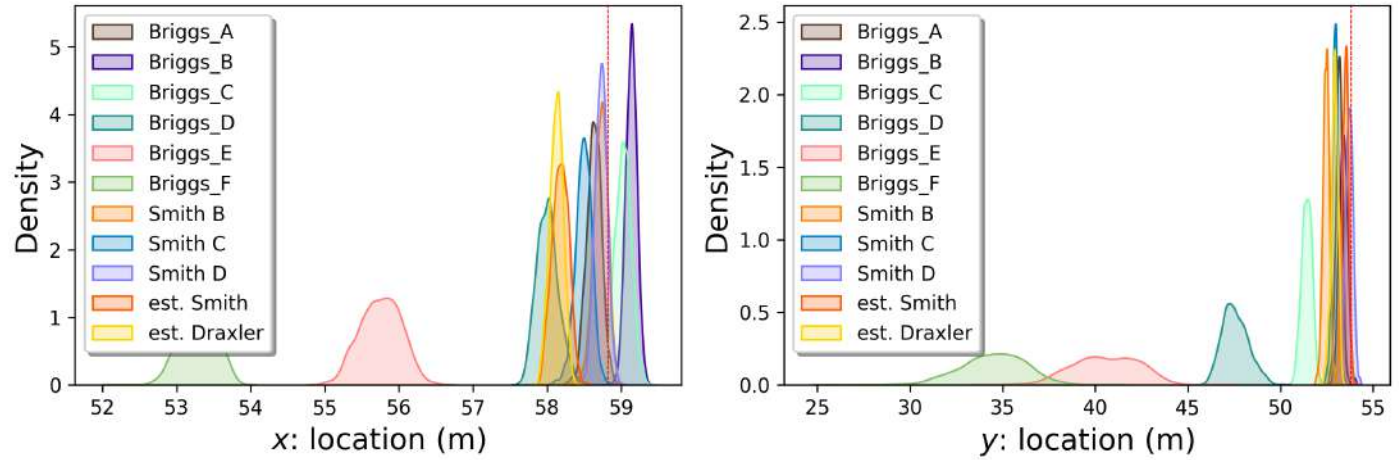


Figure 64: Source 2 location densities.

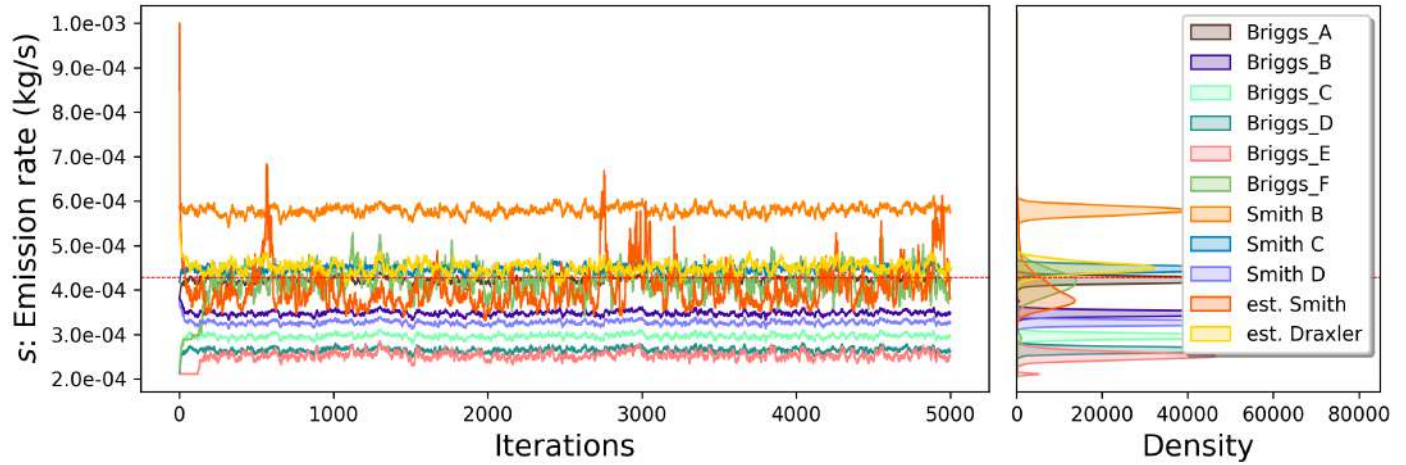


Figure 65: Source 2 emission rate.

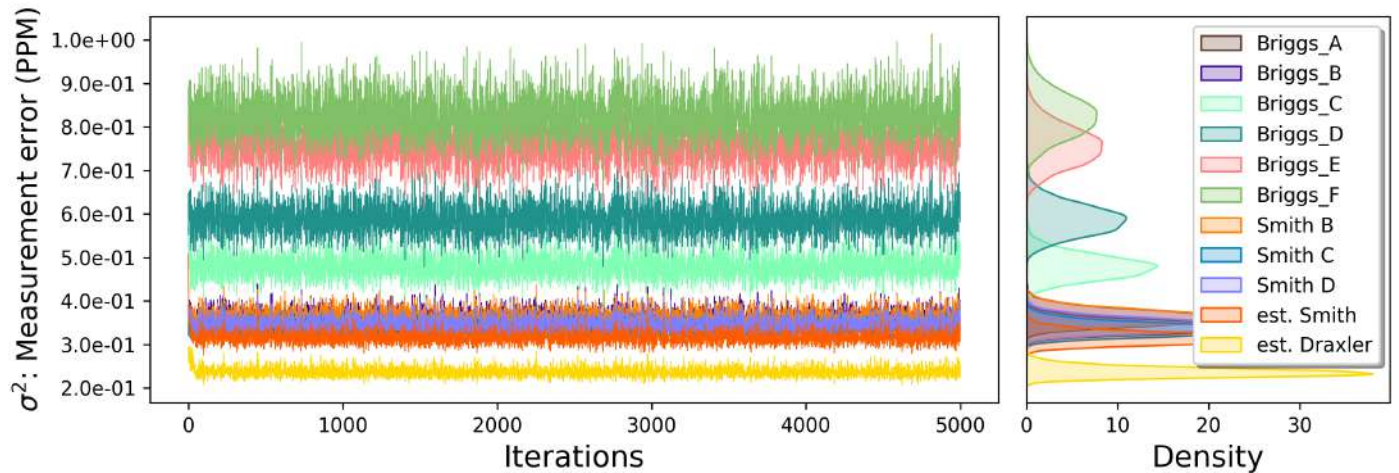


Figure 66: Source 2 measurement error variance.

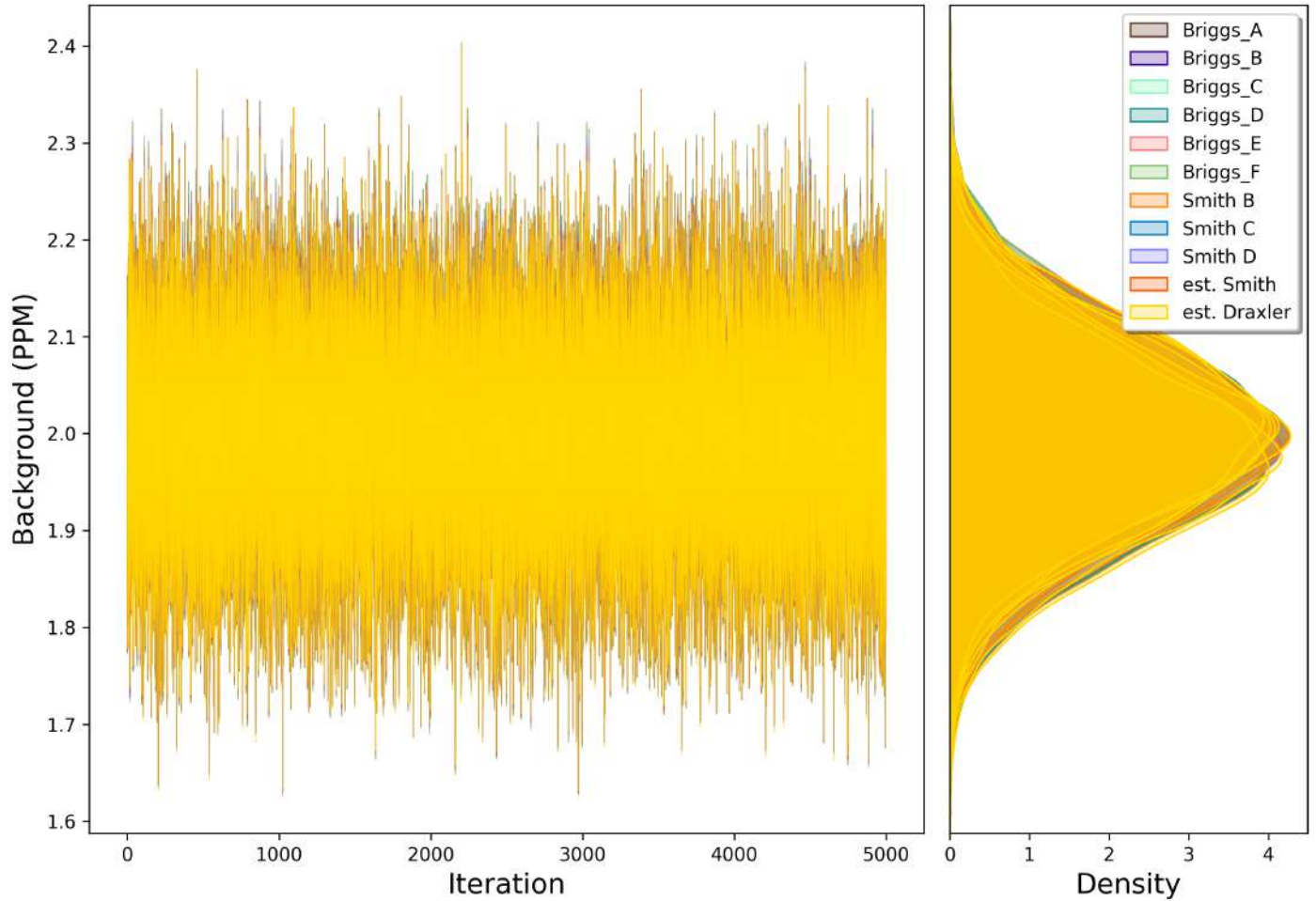
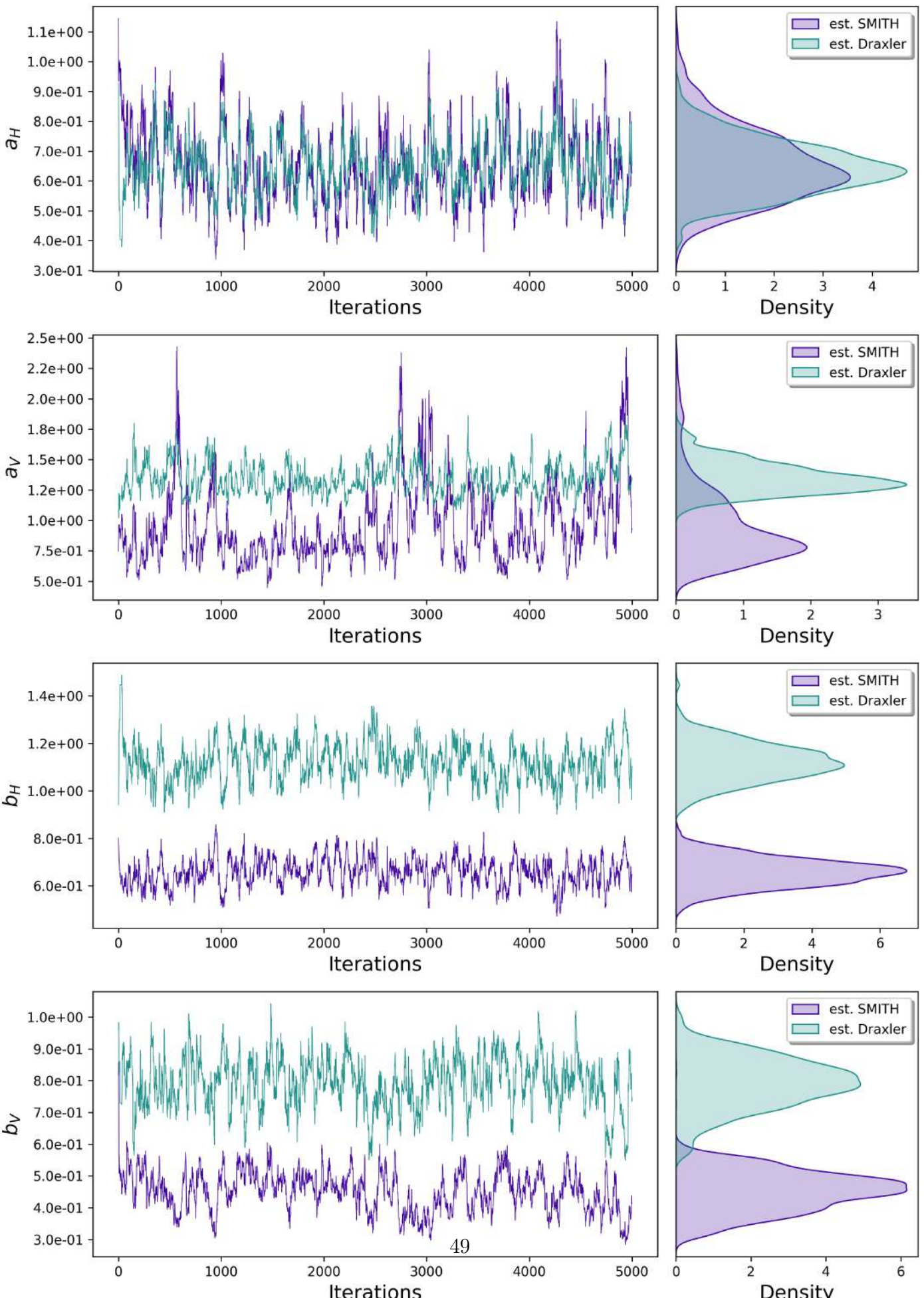


Figure 67: Source 2 background.



2.7 Chilbolton Source 3 and 4 Inversion

2.7.1 Real-data

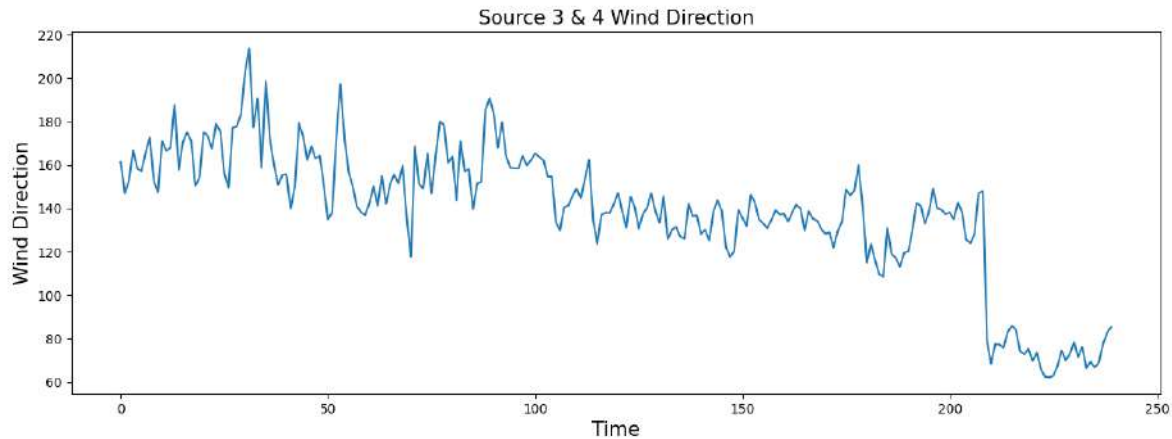


Figure 69: Source 3 and Source 4 true wind direction time series.

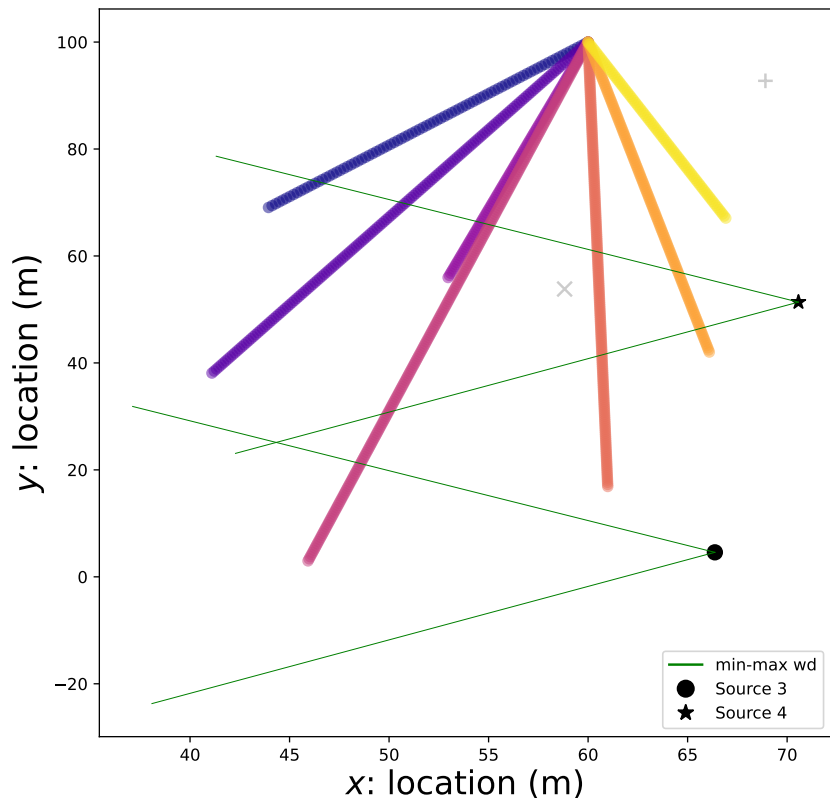


Figure 70: Source 3 and Source 4 true wind direction coverage and beam placements.

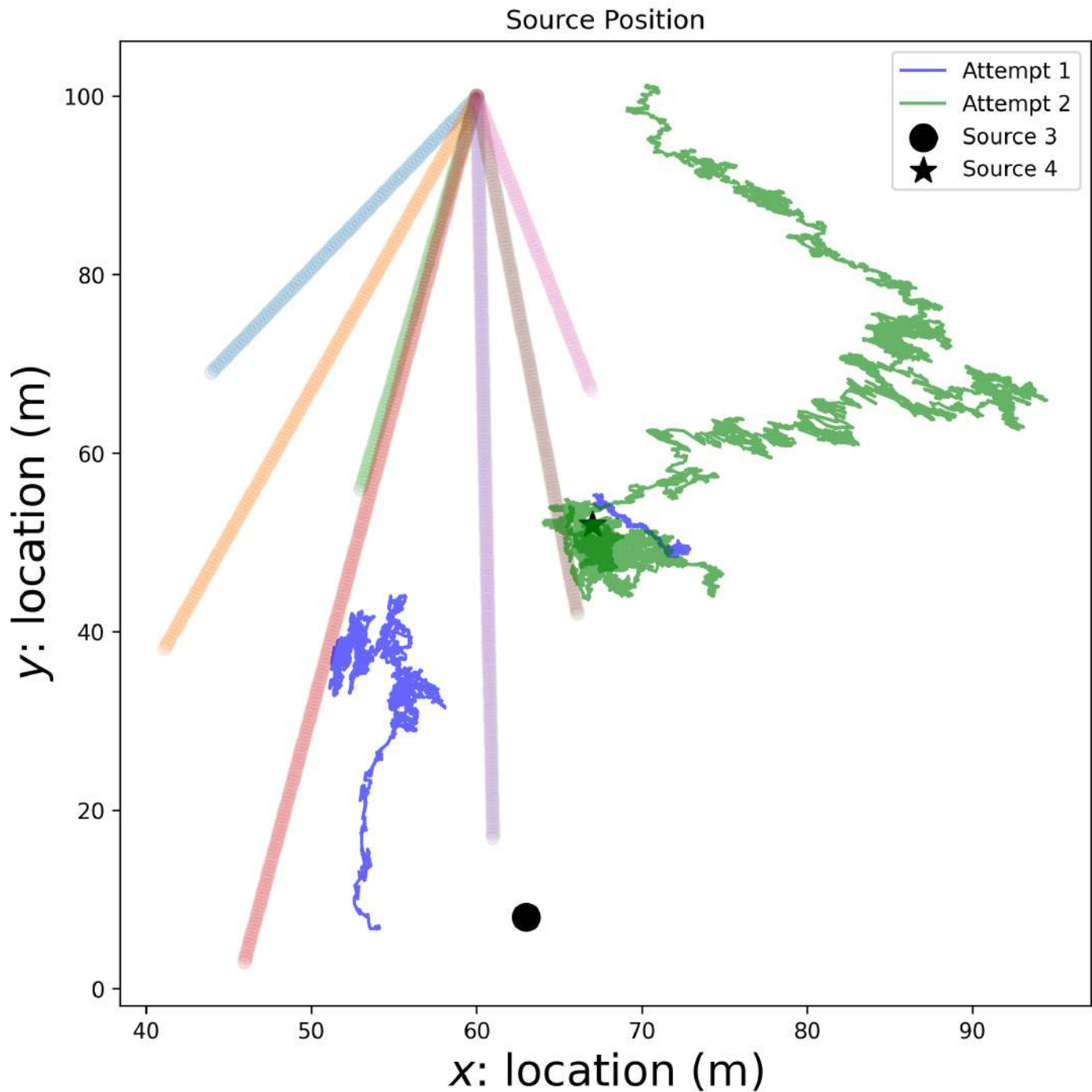


Figure 71: Source 3 and Source 4 location chains.

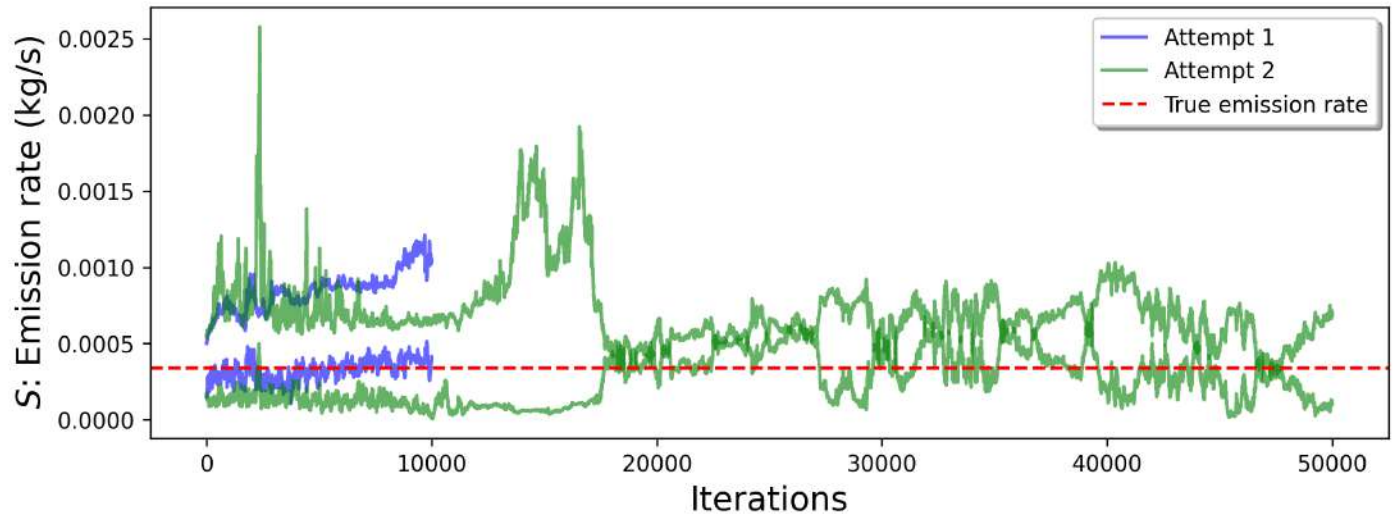


Figure 72: Source 3 and Source 4 location densities.

2.7.2 Simulation

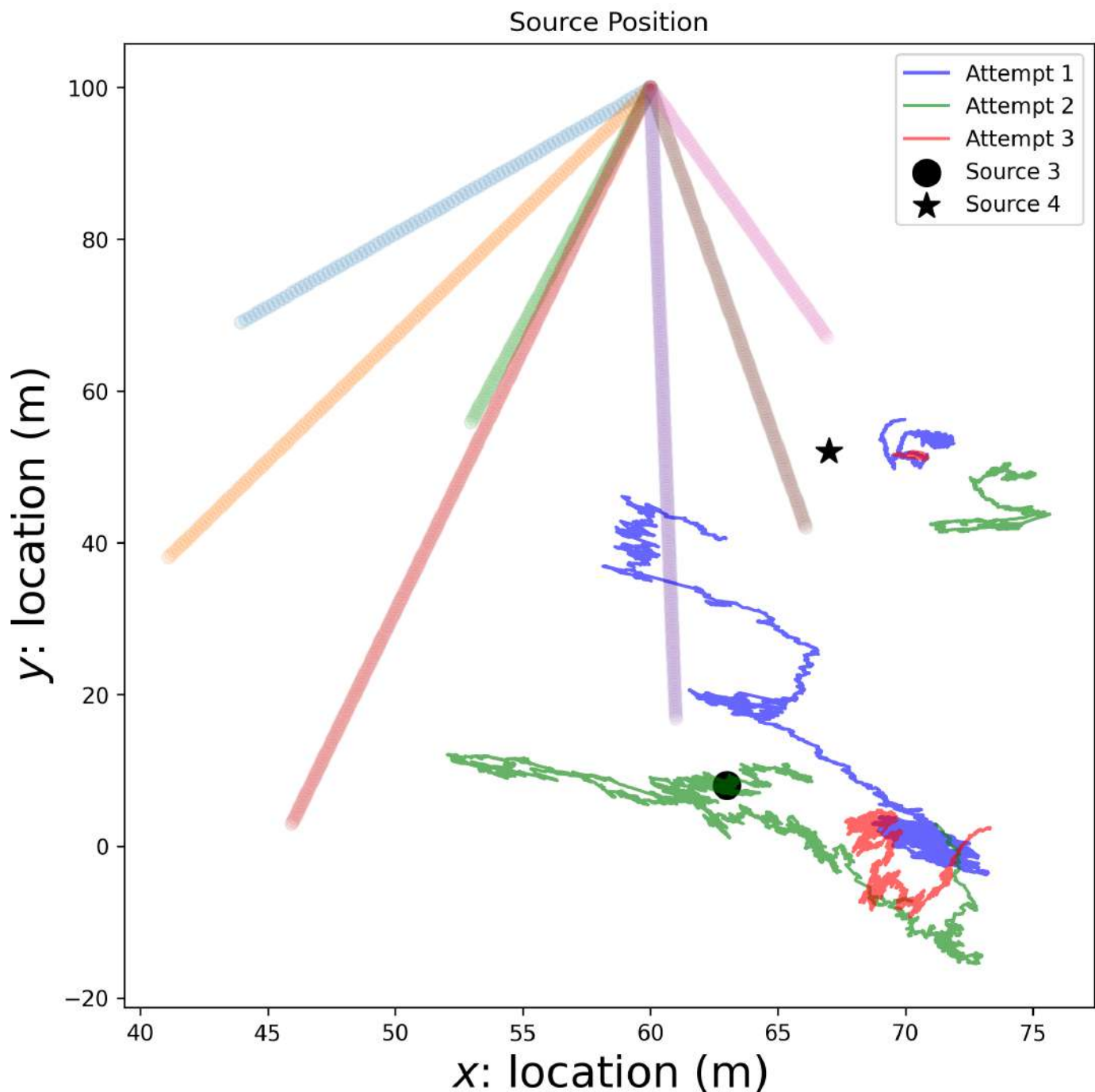


Figure 73: Source 3 and Source 4 simulation's location chains.

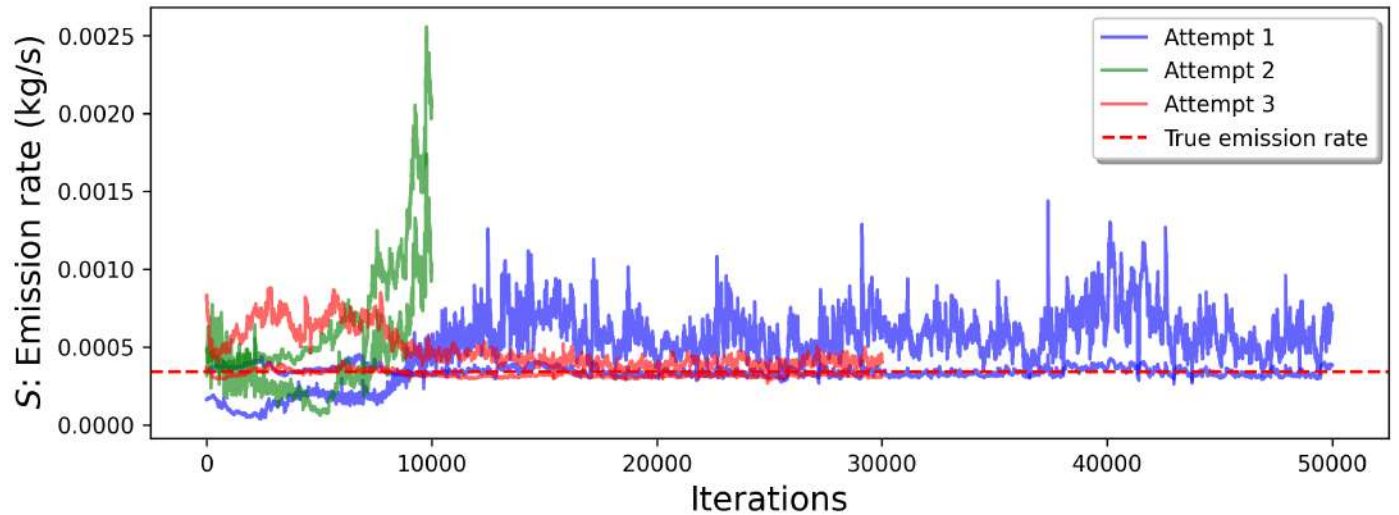


Figure 74: Source 3 and Source 4 simulation's location densities.

3 Prior Specification

In this section, we present the common set of priors used during our simulation case study and the inversion on the Chilbolton dataset. Parameters estimated using M-MALA-within-Gibbs $\{\log(s), \tilde{x}, \tilde{y}, \log(a_H), \log(a_V), \log(b_H), \log(b_V)\}$ follow a normal distribution [Girolami and Calderhead, 2011]. We chose an inverse gamma prior for the sensor measurement error variance as it is a conjugate prior and ensures that $\sigma^2 \geq 0$. Finally, we expect gas background concentrations to be normally distributed, therefore a normal prior is a sensible choice allowing efficient Gibbs sampling.

Distribution	Prior	Value	Unit
$\log(s) \sim \mathcal{N}(\mu_s, \sigma_s^2)$	μ_s	-7.5	kg/s
	σ_s^2	1.5	
$\tilde{x} \sim \mathcal{N}(\mu_x, \sigma_x^2)$	μ_x	50.0	m
	σ_x^2	25.0	
$\tilde{y} \sim \mathcal{N}(\mu_y, \sigma_y^2)$	μ_y	50.0	m
	σ_y^2	25.0	
$\log(a_H), \log(a_V) \sim \mathcal{N}(\mu_a, \sigma_a^2)$	μ_a	$\log(0.6)$	m
	σ_a^2	0.5^2	
$\log(b_H), \log(b_V) \sim \mathcal{N}(\mu_b, \sigma_b^2)$	μ_b	$\log(0.6)$	m
	σ_b^2	0.2^2	
$\sigma^2 \sim \text{Inv-Gamma}(a, b)$	a	1e-11	PPM
	b	1e-8	
$\beta \sim \mathcal{N}(\mu_\beta, \Sigma_\beta)$	μ_β	$\vec{2.0}$	PPM
	Σ_β	$0.1^2 \mathbb{I}$	

Table 4: Prior specification.

References

- Girolami, M. and Calderhead, B. (2011). Riemann manifold Langevin and Hamiltonian Monte Carlo methods. *Journal of the Royal Statistical Society Series B: Statistical Methodology*, 73(2):123–214.
- Hanna, S. R., Briggs, G. A., and Hosker Jr, R. P. (1982). Handbook on atmospheric diffusion. Technical report, National Oceanic and Atmospheric Administration, Oak Ridge, TN (USA). Atmospheric Turbulence and Diffusion Lab.
- Seinfeld, J. H. and Pandis, S. N. (2016). *Atmospheric chemistry and physics: from air pollution to climate change*. John Wiley & Sons.